Springer Series in Solid-State Sciences 168

Coulombic Fluids

Bulk and Interfaces

Bearbeitet von
Werner Freyland

1. Auflage 2011. Buch. xii, 180 S. Hardcover
ISBN 978 3 642 17778 1
Format (B x L): 15,5 x 23,5 cm
Gewicht: 456 g

Weitere Fachgebiete > Physik, Astronomie > Thermodynamik > Festkörperphysik, Kondensierte Materie

Zu Inhaltsverzeichnis

Chapter 2
Liquid Metals, Molten Salts, and Ionic Liquids: Some Basic Properties

Abstract In the second chapter, some basic concepts of statistical thermodynamics of liquids and of the nearly free electron model are introduced including quantities such as the pair distribution function $g(r)$, the structure factor $S(q)$, and the dielectric function of electronic screening. This is followed by a more detailed description of intermolecular potentials and microscopic structures of liquid metals, molten salts, and ionic liquids, both their theoretical foundation and experimental determination. A summary of the bulk phase behaviour of Coulombic fluids with emphasis on the liquid range is given. Specific thermodynamic characteristics such as undercooling, the vapour pressures of ionic liquids, or their criticality in binary mixtures are discussed. The mechanisms of electronic and ionic transport are briefly described. In the final section on interfacial characteristics, a few fundamental relations such as the Gibbs adsorption equation and the basic equations of wetting and electrowettting together with the scenario of wetting transitions are introduced. Furthermore, topics such as the stratification at liquid metal/vapour interfaces and charge ordering at electrified liquid/solid interfaces of molten salts and ionic liquids are presented. All sections contain tables with representative numbers for the properties considered.

2.1 Distribution Functions and Statistical Thermodynamics: A Brief Introduction

For the calculation of thermodynamic quantities of simple classical fluids, by either statistical thermodynamics or computer simulation methods, configurational distribution functions play a key role. They describe the microscopic structure of a fluid on the same distance scale as the intermolecular interactions. Considering a system of uniform number density, $n = N/V$, with a specific distribution of the coordinates of N molecules, $\underline{r}^N = \underline{r}_1, \underline{r}_2, \ldots, \underline{r}_N$, and of their momenta, $\underline{p}^N = \underline{p}_1, \underline{p}_2, \ldots, \underline{p}_N$, the N-particle probability density distribution function, $p_N(\underline{r}^N, \underline{p}^N)$, is defined by

W. Freyland, *Coulombic Fluids*, Springer Series in Solid-State Sciences 168,
DOI 10.1007/978-3-642-17779-8_2,

$$p_N(\underline{r}^N, \underline{p}^N) = \frac{\exp(-H_N \cdot \beta)}{Q_N}. \tag{2.1}$$

Here, $\beta = 1/kT$, with k being the Boltzmann constant, T the absolute temperature, and H_N and Q_N denote the total energy or Hamiltonian and the partition function of the system, respectively. The Hamiltonian has the usual form,

$$H_N(\underline{r}^N, \underline{p}^N) = \sum_{i=1}^{N} \underline{p}_i^2/2m + \phi(\underline{r}^N), \tag{2.2}$$

where $\phi(\underline{r}^N)$ is the total potential energy of the system. It is assumed that all particles have the same mass m. With the constraints that the number of molecules, N, the temperature, T, and the volume, V, are constant, the canonical partition function Q_N is given by – see e.g. [2.1]:

$$Q_N = \frac{1}{N!h^{3N}} \int \cdots \int \exp(-\beta \cdot H_N(\underline{r}^N, \underline{p}^N))\mathrm{d}\underline{r}^N \mathrm{d}\underline{p}^N, \tag{2.3}$$

with h being the Planck constant. Knowing the distribution function p_N, the ensemble average of any property $X = X(\underline{r}^N, \underline{p}^N)$, in principle, can be calculated according to

$$\langle X \rangle = \int \cdots \int X(\underline{r}^N, \underline{p}^N) \times p_N(\underline{r}^N, \underline{p}^N)\mathrm{d}\underline{r}^N \mathrm{d}\underline{p}^N. \tag{2.4}$$

A solution of integrals like those in (2.3) or (2.4) requires an analytical form for $\phi(\underline{r}^N)$. To this end, numerous approaches have been developed; see e.g. [2.1]. A simple and often used approximation is that by pair potentials $\phi_{ij}(\underline{r}_{ij})$,

$$\phi(\underline{r}^N) = \sum_{i>j=1}^{N} \phi_{ij}(\underline{r}_{ij}) + \Delta\phi, \tag{2.5}$$

where $\underline{r}_{ij} = \underline{r}_i - \underline{r}_j$ and the correction term $\Delta\phi$ summarizes all higher order contributions to the potential energy.

In the discussion of the local microscopic structure of simple liquids – i.e. liquids composed of identical particles with no internal structure and where the force between two particles 1 and 2 depends only on the distance $r_{12} \equiv r$ – the radial pair distribution function, $g(r)$, is of special interest. It is derived from $p_N(\underline{r}^N, \underline{p}^N)$, (2.1), by integrating the momenta out and averaging over the positions of the remaining $N-2$ molecules; this yields the two-particle distribution function, see also [2.2],

$$g_2\left(\underline{r_1}, \underline{r_2}\right) = V^2 \int \cdots \int \frac{\exp\left(-\beta \cdot \phi\left(\underline{r}^N\right)\right)}{Q_N^{\mathrm{C}}} \mathrm{d}\underline{r}_3 \cdot \mathrm{d}\underline{r}_4 \cdots \mathrm{d}\underline{r}_N, \tag{2.6}$$

where Q_N^C is the configurational partition function. It is obtained from (2.3) after integration of the momenta $\underline{p}^N$ and dividing Q_N by this integral. The distribution function $g_2\,(\underline{r}_1, \underline{r}_2)$ defines the relative probability of two molecules 1 and 2 being found simultaneously at $\underline{r}_1$ and $\underline{r}_2$.

According to the definition in (2.6), g_2 is dimensionless. If spherical symmetry can be assumed, the radial pair distribution function, $g(r)$, results,

$$g(r) = \frac{n(r)}{4\pi n r^2 \mathrm{d}r}. \tag{2.7}$$

Here, $n(r)$ is the number of molecule centres in a spherical shell of radius r and thickness dr surrounding an arbitrary molecule at the centre. Within the pair potential approximation, another simple relation for $g(r)$ results from (2.6):

$$g(r) = \exp(-\beta\phi(\mathrm{r})), \tag{2.8}$$

where $\phi(r)$ stands for $\phi_{ij}(r_{ij})$. Strictly speaking, this equation only holds in the limit of low densities where $\Delta\phi \to 0$ in (2.5). On the other hand, for dense fluids with $\Delta\phi \neq 0$, the effect of higher order interactions can be taken into account by introducing the so-called potential of mean force, $\phi_{\mathrm{eff}}(r)$. The corresponding radial pair distribution function is as follows:

$$g(r) = \exp(-\beta \cdot \phi_{\mathrm{eff}}(r)), \tag{2.9}$$

which, in first approximation, describes contributions of nearest and second nearest neighbours. An illustration of the behaviour of the radial pair distribution function of a dilute fluid (gas) in comparison with that of a dense liquid is presented in Fig. 2.1.

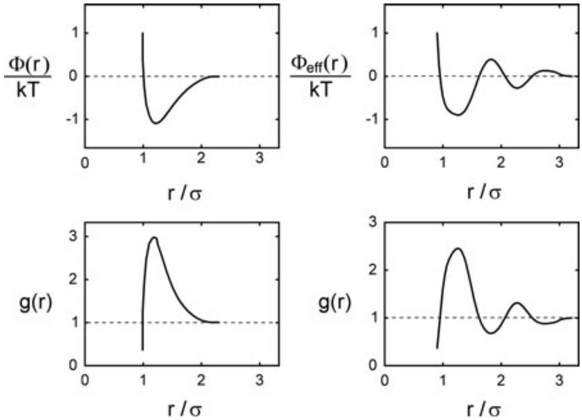

Fig. 2.1 *Upper panel*: Schematic drawing of pair potential, $\phi(r)$, and potential of mean force, ϕ_{eff}, vs. distance in units of the hard-sphere diameter σ; *lower panel*: corresponding radial pair distribution functions, $g(r)$

Experimentally, the pair distribution function $g(r)$ can be determined from X-ray or neutron diffraction measurements of the structure factor, $S(q)$; see Sect. A.1. These quantities are related by Fourier transformation according to:

$$S(q) = 1 + 4\pi \cdot n \int_0^\infty (g(r) - 1) \frac{\sin qr}{qr} r^2 \mathrm{d}r. \tag{2.10}$$

In the limit $q \to 0$ the structure factor obeys the relation,

$$S(0) = \kappa_\mathrm{T} n k T, \tag{2.11}$$

where κ_T is the isothermal compressibility. This thermodynamic limit is often used as an independent check of the correction of scattering data.

In this chapter, some basic relations of statistical thermodynamics and microscopic structure of simple liquids have been summarized, which are of interest in the following. For a detailed presentation of *the theory of simple liquids*, reference is given to the classical book by Hansen and McDonald [2.3].

2.2 Interatomic Interactions and Microscopic Structures

2.2.1 Liquid Metals

The physics of metallic matter, in the solid and liquid state, is described in many monographs and textbooks, of which the following references are especially recommended for further studies [2.4–2.7]. Here, we confine to a short introduction of simple characteristics of the metallic state and briefly sketch the main approximations leading to screened effective pair potentials in metals.

Metals, in general, may be considered as a two-component system made up of ions and delocalized conduction electrons, whereby the latter originate from the valence electrons of the metal atoms. The volume fraction occupied by the ion cores is usually small so that most of the space in simple metals is available for the conduction electrons – for example, in solid or liquid alkali metals at conditions near their normal melting point only about 15% of the specific volume is taken by the ion cores. In the simplest approximation, the conduction electron states are treated as a gas of free and independent electrons – free electron (FE) model. Thus, the eigenstates of these electrons are the solutions of the time-independent Schrödinger equation,

$$\frac{-\hbar^2}{2m_\mathrm{e}} \nabla^2 \Psi(\underline{r}) = E\, \Psi(\underline{r}), \tag{2.12}$$

with the periodic boundary conditions:

$$\Psi(x + L, y, z) = \Psi(x, y, z), \tag{2.13}$$

and similar for y, z. Here, the electron of mass m_{e} is contained in a 3D cube of volume $V = L^3$. The eigenfunctions are running plane waves,

$$\Psi_{\underline{k}}(\underline{r}) = \frac{1}{\sqrt{V}} \exp(\mathrm{i}\,\underline{k}\,\underline{r}), \tag{2.14}$$

with energy

$$E(\underline{k}) = \frac{\hbar^2 k^2}{2m_{\mathrm{e}}}. \tag{2.15}$$

Since $\Psi_{\underline{k}}\,(\underline{r})$ is also a solution of the momentum operator, $\hbar\underline{k}$ has the meaning of a momentum. Due to the boundary conditions, the wave vector $\underline{k}$ has only certain discrete values of the form: $k_x = 2\pi n_x/L$, $k_y = 2\pi n_y/L$, and $k_z = 2\pi n_z/L$, with $n_i =$ integers. For the ground state ($T = 0\mathrm{K}$) of N noninteracting electrons, we begin by placing two electrons in the lowest energy state of $E = 0$ with $\underline{k} = 0$ and continue up to the highest electron level with energy E_{F} (Fermi energy) and wave vector k_{F} (Fermi wave vector). The factor 2 results from the Pauli exclusion principle, i.e. for each $\underline{k}$ there are two states, one for each spin direction. Within a sphere of radius k_{F}, the number of occupied states is $N = 2(4\pi k_F^3/3)/(2\pi/L)^3$ and thus k_{F} can be expressed by

$$k_{\mathrm{F}} = \left(\frac{3\pi^2 N}{V}\right)^{1/3}. \tag{2.16}$$

In a similar way, the number of states per energy unit or the density of states, $n\,(E)$, can be derived; see e.g. [2.4]:

$$n(E) = \frac{3}{2}\left(\frac{n}{E_{\mathrm{F}}}\right)\left(\frac{E}{E_{\mathrm{F}}}\right)^{1/2}, \tag{2.17}$$

where $n = N/V$.

At finite temperatures, the occupation of the electronic energy levels is determined by the Fermi–Dirac distribution function,

$$f(E) = \left(\exp\left(\frac{(E-\mu)}{kT}\right) + 1\right)^{-1}, \tag{2.18}$$

where μ is the chemical potential of electrons with $\mu \equiv E_{\mathrm{F}}$ for $T = 0$. With the aid of $n(E)$ and $f(E)$ the internal energy U of the free electron gas is given by

$$U = V \int E\, n(E) f(E) \mathrm{d}E, \tag{2.19}$$

which yields for the average energy per electron in the ground state: $\langle E\rangle = (3/5) \cdot E_{\mathrm{F}}$.

The free electron or Sommerfeld theory of metals successfully accounts for some metallic properties including the temperature dependence of the specific heat at low temperatures and the high metallic conductivities, at least qualitatively. In this theory, the ions play no role with exception of maintaining overall charge neutrality. However, in many respects, this model is unrealistic! In the neighbourhood of the ion cores, the conduction electrons clearly interact with the positively charged ions. Nevertheless, for the following reasons, the electrons do not experience the full Coulomb attraction, but only a weak potential that may be approximated by a weak, nearly constant pseudopotential – nearly free electron (NFE) model. The first argument is that due to the Pauli exclusion principle the conduction electrons are expelled from the region of core electrons where the Coulomb attraction would be strongest. Secondly, outside the ion core the Coulomb interaction a conduction electron experiences is strongly screened by the rest of electrons. So the interactions between the ions and the conduction electrons can be treated as a weak perturbation (NFE model). In the following, the effect of screening is discussed in more detail; see also [2.4].

We first consider a positively charged particle with charge density $\rho_+(\underline{r})$ at a fixed position inside the electron gas. The electrostatic potential, $\phi_+(\underline{r})$, resulting from ρ_+ itself is given by Poisson's equation:

$$\nabla^2\phi_+(\underline{r}) = -4\pi\,\rho_+(\underline{r}). \tag{2.20}$$

The Fourier transform of (2.20) is as follows:

$$q^2\phi_+(\underline{q}) = 4\pi\,\rho_+(\underline{q}). \tag{2.21}$$

Very similar relations hold for the total potential $\phi(\underline{r})$ produced by both the positively charged particle and the induced cloud of screening electrons, $\rho_-(\underline{r})$. If the positive charge is an ion, the system of ion plus screening cloud of electrons sometimes is called a *pseudoatom*, though the screening electrons are not bound to the ion. To quantify the effect of screening, a linear relation between the Fourier components of $\phi(\underline{r})$ and $\phi_+(\underline{r})$ is assumed,

$$\phi\left(\underline{q}\right) = \varepsilon\left(\underline{q}\right)^{-1}\phi_+\left(\underline{q}\right), \tag{2.22}$$

where the reduction of ϕ_+ is described by the wave vector dependent dielectric function, $\varepsilon(q)$. For sufficiently weak ϕ, the linear relation of (2.22) should hold. The problem of screening is now the determination of $\varepsilon(q)$. In quantum theoretical calculations, the quantity that is more directly accessible is the charge density $\rho_-(\underline{r})$ induced in the electron gas by $\phi(\underline{r})$. Assuming again a linear relation between ρ_- and ϕ, their Fourier transforms satisfy the equation:

$$\rho_-\left(\underline{q}\right) = \chi\left(\underline{q}\right)\phi\left(\underline{q}\right). \tag{2.23}$$

From (2.21) and the corresponding Fourier transform of $\nabla^2\phi(\underline{r}) = -4\pi\,(\rho_+(\underline{r}) + \rho_-(\underline{r}))$, the following relation between $\varepsilon(\underline{q})$ and $\chi(\underline{q})$ results:

$$\varepsilon(\underline{q}) = 1 - \left(\frac{4\pi}{q^2}\right)\chi(\underline{q}) = 1 - \frac{(4\pi/q^2)\rho_-(\underline{q})}{\phi(\underline{q})}. \tag{2.24a}$$

The determination of $\chi(\underline{q})$ and thus of $\varepsilon(\underline{q})$ now concentrates on the calculation of $\rho_-(\underline{q})$. This, in principle, can be obtained from the electron pseudowave functions using ϕ as the potential in the Schrödinger equation. Here, we consider two approximate solutions. In the Thomas–Fermi approximation, the dielectric constant is as follows:

$$\varepsilon(\underline{q}) = \frac{1 + k_{\mathrm{TF}}^2}{q^2}, \tag{2.24b}$$

where $k_{\mathrm{TF}} = 0.815(r_{\mathrm{s}}/a_{\mathrm{B}})^{1/2} \cdot k_{\mathrm{F}}$ is the Thomas–Fermi screening length, $r_{\mathrm{s}} = (3/4\pi n)^{1/3}$, and a_{B} = Bohr radius. Since $r_{\mathrm{s}}/a_{\mathrm{B}}$ is about 2–6 for metals, k_{TF} is of the order of k_{F}. To illustrate the effect of $\varepsilon(\underline{q})$ on $\phi_+(\underline{r})$, we consider as an example a point charge with $\phi_+(\underline{r}) = Q/r$ and with the Fourier transform $\phi_+(\underline{q}) = 4\pi Q/q^2$. The total potential $\phi(\underline{q})$ is then as follows:

$$\phi(\underline{q}) = \varepsilon(\underline{q})^{-1}\phi_+(\underline{q}) = \frac{4\pi\,Q}{(q^2 + k_{\mathrm{TF}}^2)}, \tag{2.25}$$

which has the inverse Fourier transform

$$\phi(\underline{r}) = \left(\frac{Q}{r}\right) \cdot \exp\left(-k_{\mathrm{TF}} \cdot r\right), \tag{2.26}$$

i.e. in the Thomas–Fermi approximation, the Coulomb potential is exponentially screened over a distance of the order of k_{F}^{-1}.

The second approximation, first given by Lindhard [2.8], is a first-order perturbation calculation of $\rho_-(\underline{r})$ within the Hartree model. In this case, the screening of a point charge at large distances takes the following form:

$$\phi(r) \sim W(2k_{\mathrm{F}})^2 \cdot (2k_{\mathrm{F}}r)^{-3}\cos(2k_{\mathrm{F}}r). \tag{2.27}$$

The amplitude of the so-called Friedel oscillations of $\phi(r)$ is determined by the magnitude of the screened pseudopotential $W(\underline{q})$ at $q = 2k_{\mathrm{F}}$. It may also be noted that the screening in the Lindhard approximation decays more weakly with r in comparison with the Thomas–Fermi approximation. With the knowledge of electronic screening, the construction of the effective interionic or pair potential $\phi(R)$[1] in pure metals is straightforward. Effective here means that the interionic interaction

---

[1] In the following, we also use R for the intermolecular distance in the pair potentials.

is mediated by the electron gas. It is assumed that at low R a Thomas–Fermi type repulsion prevails, whereas at intermediate and large R the attraction is given by an oscillatory potential. Thus, $\phi(R)$ can be approximated by

$$\phi(R) = \frac{2Z^2}{R}\exp(-k_{\mathrm{TF}}R) + W(2k_{\mathrm{F}})^2\frac{\cos(2k_{\mathrm{F}}R)}{(2k_{\mathrm{F}}R)^3}, \tag{2.28}$$

i.e. the ion core is approximated by a point charge. It is worth noting that this pair potential, unlike, for instance, a conventional Lennard–Jones potential, depends on the volume V, because k_{F} is a function of V. Therefore, a better specification of ϕ should be $\phi(R; V)$, which implies that in metals a state-dependent potential has to be considered. The characteristic behaviour of $\phi(R; V)$ is shown in Fig. 2.2 for the examples of Na and Al. The respective potentials have been calculated using the same empty-core pseudopotentials but with different screening of the Coulomb repulsion – for further details see [2.5].

A first test of effective pair potentials of metals was performed by Rahman [2.9]. By employing a potential of Price et al. [2.10], he calculated the static structure factor of liquid Rb by molecular dynamic simulations and found good agreement with experimental results from neutron diffraction [2.11].This is shown in Fig. 2.3.

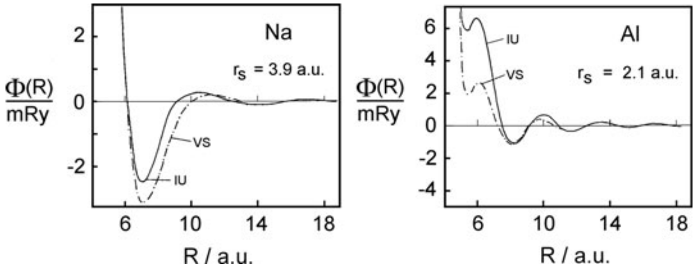

Fig. 2.2 Effective pair potentials for Na (*left*) and Al (*right*); the respective different curves correspond to different screening of the Coulomb repulsion – see Hafner [2.5]. Copy right permission (2010) by Springer Publishers

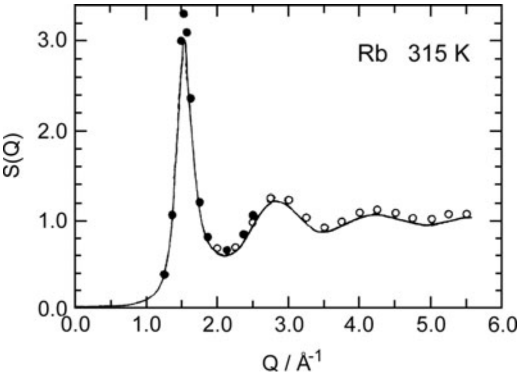

Fig. 2.3 Structure factor, $S(Q)$, of liquid Rb as obtained from MD calculations (*full line*) and neutron diffraction (*full* and *open symbols*). Figure adopted from [2.11] with permission from Copley and Rowe; copyright permission (2010) by the American Physical Society

2.2.2 Molten Salts and Ionic Liquids

In this section, we concentrate on the characteristic structural properties of molten salts and ionic liquids. They consist of oppositely charged species, but the character of these species varies from classical ions in the typical molten salts to charged polyatomic molecules in ionic liquids. The prototype of molten salts are fused alkali halides that contain closed-shell alkali and halogen ions and which exhibit high melting temperatures around 1,000 K. On the other hand, most ionic liquids have a polyatomic organic cation and an inorganic or organic anion. They typically melt near room temperature and, therefore, in the beginning, were also named room temperature or ambient temperature molten salts [2.12, 2.13]. The first ionic liquids, which were synthesized and characterized around 1980, were based on pyridinium [2.14] and imidazolium [2.15], [2.16] cations; see Fig. 2.4; mixtures of their chlorides with $AlCl_3$ become liquid over a wide range of compositions below room temperature; see e.g. Fig. 2.13 in Sect. 2.3. Over the last two to three decades, a large variety of ionic liquids have been synthesized, including so-called air and water stable melts, and have been applied in different fields such as organic, inorganic, or polymer synthesis, electrochemistry, catalysis, and various industrial processes – for a comprehensive description of properties, synthesis, and applications, see [2.13].

On melting of an alkali halide crystal, the ionic short-range order essentially remains. This is demonstrated by the partial pair distribution functions $g_{+/-}(R)$ for the example of molten RbCl in Fig. 2.5, which have been obtained from neutron diffraction experiments with isotopic substitution [2.17]. On comparing the coordination of unlike and like ions, a remarkable short-range order, i.e. alternation of charges, in the ionic melt is apparent. This also implies that ionic screening is oscillatory rather than monotonously decaying as in concentrated electrolytes. The first peak in $g_{+/-}(R)$, which marks the correlation of unlike ions, is rather pronounced and the first minimum is quite deep. This last observation suggests a slow exchange rate of ions between the first-neighbour shell and the bulk liquid. From MD calculations, a displacement time of two unlike ions of the order of several picoseconds has been estimated; see also [2.18]. The nearest neighbour distance, $R_{+/-}$, defined by the sharp maximum in $g_{+/-}(R)$, is slightly smaller than in the solid; see Table 2.1. This peak is asymmetrically broadened so that the corresponding coordination number $N_{+/-}$ is not clearly defined. If one mirrors the left part of the peak at $R_{+/-}$, this yields an average number of unlike ions in close contact of $\sim$4 [2.18]. On the other hand, integration of the peak up to the first minimum yields an average nearest neighbour coordination number of $\sim$6, which is comparable with the crystal value;

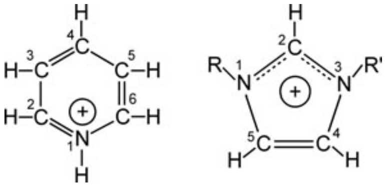

Fig. 2.4 Pyridinium (*left*) and imidazolium cation

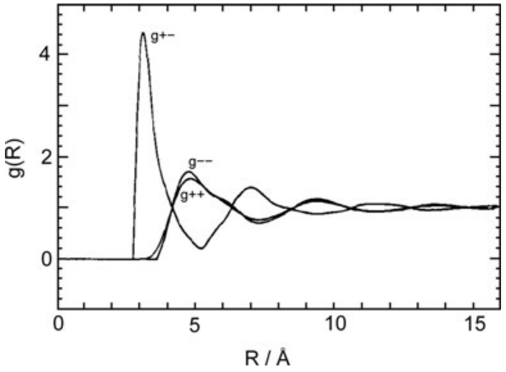

Fig. 2.5 Smoothed partial pair distribution functions of molten RbCl obtained by neutron diffraction. Reprinted with permission from [2.17]; copyright permission (2010) by Taylor & Francis

Table 2.1 Structural properties of solid (s) and liquid (l) alkali halides near the melting temperature, T_m, at atmospheric pressure: $R_{+/-}$ = nearest neighbour distance; $N_{+/-}$ = coordination number of nearest neighbours; $\Delta V/V$ = fractional volume change

	T_m/K	$R^{(s)}_{+/-}$/Å	$N^{(s)}_{+/-}$	$R^{(l)}_{+/-}$/Å	$N^{(l)}_{+/-}$	$\Delta V/V\%$
NaCl	1,081 (a)	2.814 (a)	6	2.78 (b)	~5.8 (b)	25 (e)
KCl	1,045 (a)	3.139 (a)	6	3.06 (c)		17.3 (e)
RbCl	990 (a)	3.27 (a)	6	3.18 (d)	~6.9 (d)	14.3 (e)

References in brackets: a = [2.19]; b = [2.20]; c = [2.21]; d = [2.18]; e = [2.22]; the $R^{(s)}_{+/-}$ values are taken at room temperature, the uncertainty of the liquid values is ±0.05 Å

see Table 2.1. Possibly, the reduced number of 4 can explain the relatively large expansion of the alkali halides on melting. The characteristic structural changes described here for the example of RbCl agree with further neutron diffraction studies of NaCl [2.20] and KCl [2.21] at conditions near the melting point.

Starting from the close similarity in the local microscopic structures of crystalline and molten alkali halides, this suggests the use of similar interionic model potentials to calculate the structural and thermodynamic properties of molten metal halides. The most widely applied form is the Born–Mayer potential, see e.g. [2.23], which is given by

$$\phi_{\mathrm{ij}}(R) = A_{\mathrm{ij}} \exp\left(\left(R_i + R_j - R\right)/\alpha_{ij}\right) + Q_i Q_j/R - C_{ij} R^{-6} - D_{ij} R^{-8}. \tag{2.29}$$

Here, the indices i and j refer to a cation or an anion and ϕ_{ij} is the potential energy of a pair of ions i and j. It is a pairwise additive potential where the first term in (2.29) describes the short-range Born–Mayer type repulsion due to overlapping orbitals on neighbouring ions, which increases nearly exponentially with decreasing interionic distance. The Coulombic part describes the attraction between oppositely charged ions i and j. For an analysis of the parameters R_i, R_j, and α_{ij}, see the article by Fumi and Tosi [2.24]. The R_i for a given crystal structure have the meaning of ionic radii. The van der Waals terms with negative signs represent dipole–dipole and dipole–quadrupole interactions and typically give a small correction of the cohesive energy.

Starting in the 1970s, numerous calculations of the microscopic structure and thermodynamic properties of molten salts have been performed employing pair potentials of the type in (2.29) including rigid and polarizable ions; see also references [2.18] and [2.22]. In general, the calculated internal energies of alkali halide melts agree well with experimental results, often within ±1% [2.25]. Theoretical work on the local ionic structures includes computer simulation studies – molecular dynamics (MD) and Monte Carlo (MC) simulations – as well as hypernetted chain (HNC) and mean spherical (MSA) approximations; see also [2.22]. One of the first MD simulations was reported by Woodcock and Singer for molten KCl [2.26, 2.27]. Good agreement with experimental data was found for both the partial radial distribution functions and the thermodynamic quantities such as internal energy, compressibility, and molar heat capacity. As an example, Fig. 2.6 shows for molten NaCl a comparison of experimental $g_{ij}(R)$ from neutron diffraction [2.28] with theoretical studies, both simulation results with a rigid ion model [2.29] and HNC calculations [2.30]. Although the agreement between the different datasets is satisfactory, there is a slight discrepancy between experiment and theory as for the position and width of the first peak in $g_{+/-}(R)$. Yet, in general, calculations based on a Born–Mayer type interionic potential give satisfactory results for the local ionic structures and thermodynamic functions of molten alkali halides.

Proceeding to other metal halide melts, more complex binding characteristics and variations in the microscopic ionic structures have to be considered. First, we discuss the example of liquid CuCl. In the solid state, CuCl crystallizes in the zincblende structure at lower temperature with fourfold coordination. This low number is also found in the liquid state from pair distribution functions determined by neutron diffraction with isotopic substitution; see Fig. 2.7 and [2.31]. On comparing the

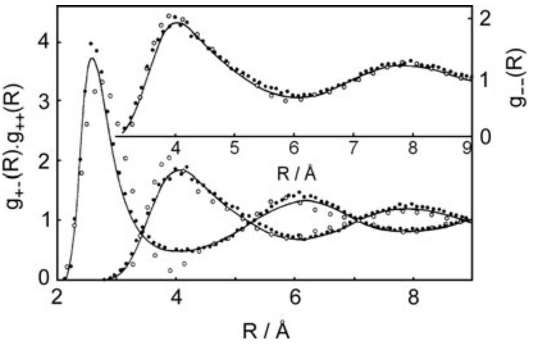

Fig. 2.6 Partial pair distribution functions of molten NaCl at conditions near the melting point, from neutron diffraction measurements (*open symbols*), simulation calculations (*full symbols*), and HNC theory (*full lines*). Reprinted with permission from [2.18]; copyright permission (2010) from IOP Publishing Ltd

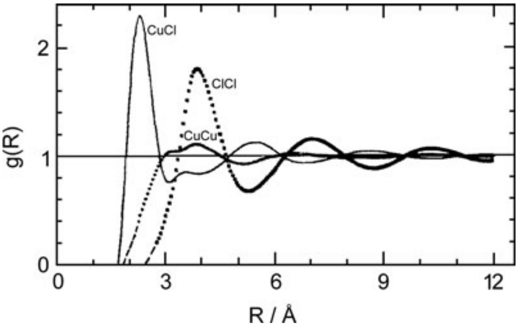

Fig. 2.7 Smoothed data of the partial pair distribution functions, $g_{ij}(R)$, of liquid CuCl at 500°C from neutron diffraction experiments with isotopic substitution. Reprinted with permission from [2.31]; copyright permission (2010) by Taylor & Francis

$g_{ij}(R)$ with those in a typical alkali halide melt, the following differences are apparent: (1) There is an asymmetry between charge ordering in g_{ClCl} and g_{CuCu} at larger R. (2) Most striking is the observation that Cu^+ ions penetrate deeply into the coordination shell of unlike first neighbours; the shortest Cu−Cu distance is comparable with the shortest Cu − Cl distance. These observations are not consistent with simple ionic interactions and are explained as follows. The monovalent Cu^+ ion has an outer subshell of ten d-electrons, a small ionic radius and large electronic polarizability in comparison with an alkali ion such as K^+. In contact with a highly polarizable Cl^- anion, covalent contributions in the $\mathrm{Cu}^+ - \mathrm{Cl}^-$ interaction have to be taken into account accompanied by a low coordination. Thus, the electronic structures of the ions can play an important role. Similar considerations apply for the interpretation of the structure of silver halide melts; see also [2.18].

In the case of divalent metal halides – metal ions of group IIA and IIB – a classification of the bonding characteristics has been predicted based on valence electron orbital radii [2.32]. Accordingly, bond ionicity should increase going from the lighter metal ions such as Zn^{2+} or Mg^{2+} to the heavier ones. This trend is supported by the results of neutron diffraction measurements of molten chlorides: For Ba^{2+} containing salts, the coordination number of closest contact of unlike ions is reported as 6.4 ± 0.2, whereas for Zn^{2+} systems it is given by 4.3 [2.33]. For ZnCl_2, different diffraction studies in the liquid and glassy state have been published, [2.33–2.36], including a more recent analysis of the partial structure factors from total scattering data [2.37], which all agree on the following structural model. The occurrence of a prepeak in $S(Q)$ clearly indicates intermediate range ordering. This is explained by a random close packing of Cl^- ions with a coordination number of N_{ClCl} of 8–10 with the Zn^+ ions occupying tetrahedral holes. Corner sharing of the resulting ZnCl_4^{2-} tetrahedrons enables a maximum distance between Zn^{2+} ions and thus a minimum of the Zn − Zn repulsion. Further evidence for a network-like melt with bridged tetrahedral ZnCl_4^{2-} species comes from Raman spectroscopy; see e.g. [2.38], but see also the interpretation of these spectra by MD simulations [2.39]. Consistent with this structural model are also the low electrical conductivity and high viscosity of molten ZnCl_2 – see Sect. 2.4.

Recently, the structure of liquid ZnCl_2 has been studied over a wide range of pressure and temperature (up to 4.5 GPa and 1,300 K), both by X-ray diffraction

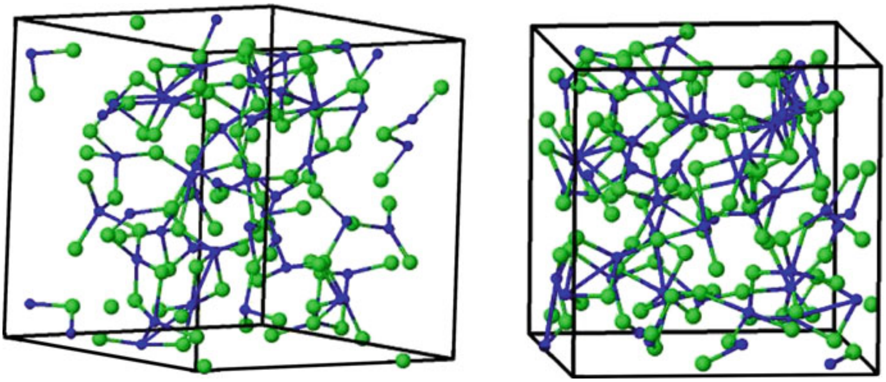

Fig. 2.8 Snapshots of MD simulations of liquid $ZnCl_2$ at 1,273 K; (*left*) covalent network regime at low pressure; (*right*) ionic liquid regime at high pressure. Reprinted with permission from [2.41]; copyright permission (2010) by Elsevier

[2.40] and by MD simulations [2.41]. The main findings of these investigations are that with increasing pressure a liquid–liquid transition occurs at higher temperatures, whereby the structure transforms from a covalent network of Cl^- ions to a dissociated ionic liquid. This structural transition is illustrated in Fig. 2.8 by two snapshots of the MD calculations.

With respect to the following discussion of the microscopic structure of ionic liquids and their mixtures with chloroaluminates, a comment on the structure of $AlCl_3$ melts is of interest. Aluminium trichloride melts at a relatively low temperature of 192°C (under pressure) [2.19] and exhibits an enormous expansion on melting of $\Delta V/V_s \sim 80\%$ [2.18]. The specific electrical conductivity is very low ($\sim 10^{-7}\ \Omega^{-1}\ \mathrm{cm}^{-1}$), comparable with that of a molecular liquid. First evidence that the melt is composed of molecular Al_2Cl_6 units came from Raman spectroscopy [2.38]. Recently, Madden et al. [2.42] have performed MD calculations of the liquid structure of $AlCl_3$ using an interaction model of polarizable ions. They found edge-sharing of tetrahedral structural units leading to the formation of charge neutral Al_2Cl_6 dimers, which they explain by the strong polarization of the Cl^- ions. Mixing of $AlCl_3$ with molten alkali halides leads to the formation of complex ion species in equilibrium, i.e. $AlCl_4^-$ and $Al_2Cl_7^-$. Raman measurements indicate that at compositions of $x_{AlCl_3} < 0.5$, the $AlCl_4^-$ tetrahedral species predominate [2.38]. These ionic species also form in mixtures of $AlCl_3$ with ionic liquids. This was shown first by Osteryoung et al. [2.14] who measured the Raman spectra of aluminium chloride-1-butyl-pyridinium melts. ^{27}Al NMR studies of the same system showed that the $AlCl_4^-$ and $Al_2Cl_7{}^-$ ions have lifetimes up to milliseconds [2.43].

Finally, for further information on the microscopic structure of metal halide mixtures and transition metal and rare earth metal halide melts, reference is given to the comprehensive reviews by Brooker and Papatheodorou [2.38] and Tosi et al. [2.44].

In comparison with molten salts, experimental research on the structural properties of ionic liquids is less advanced. In recent years, however, various computational methods have been employed to study the structure and dynamics of pure ionic liquids and their mixtures with organic solvents, inorganic salts and gases such as CO_2. Computational modelling of ionic liquids includes methods such as classical MD and MC simulations, ab initio quantum chemical, and ab initio or Car–Parrinello MD calculations. A very recent review by Lynden-Bell et al. [2.45] covers results on ionic liquids obtained by these methods. So, we concentrate here on a few topics of these computations on the structural properties. They have been performed predominantly for imidazolium-based ionic liquids and their mixtures.

The first simulation study of chloride and hexafluorophosphate salts of dimethylimidazolium and 1-ethyl-3-methylimidazolium $[C_2mim]^+$ was reported by Lynden-Bell and coworkers [2.46]. The interionic potential they used is similar to the Born–Mayer pair potential – see (2.29) – but without the quadrupolar term. Partial charges at each atomic centre were determined from ab initio calculations of individual cations and anions. Bond lengths and angles were kept fixed except those formed between the $N-C-H$ atoms in the methyl groups. Calculations were performed both with an explicit atom model and with a so-called united atom model where the carbon atoms and the hydrogen atoms are lumped. This potential model or force field was tested on the crystal structures of the respective compounds. Results of these calculations for the liquid structures at 400 K are shown in Fig. 2.9. A pronounced first peak is visible in the cation–anion radial pair distribution function $g_{+/-}(R)$, which is similar for the explicit atom and united atom model calculations for the chloride melts. In the case of the PF_6^- salt, this peak is shifted towards larger distances corresponding to the bigger anion size. The data also indicate a long-range charge ordering up to distances of $\sim$1.5nm. A more detailed picture of the anion distribution around the imidazolium cation is given by the 3D distribution functions in Fig. 2.9b, c. Apparently the highest probability for the chloride ion is near the C_2 hydrogen, which is the most acidic site and the region of highest positive charge. A view along the molecular symmetry axis down the $C-H$ bond (Fig. 2.9c) illustrates that the highest probability of the Cl^- ion is above and below the plane of the molecule.

In the years following 2001, various force fields with essentially the same functional form but with different parameters have been developed and critically analyzed for imidazolium-based ionic liquids; see [2.45]. The corresponding simulations essentially confirm the structural results described above. In several publications, Voth and coworkers have studied the effect of various alkyl side-chain lengths on the mesoscopic structure of imidazolium nitrate melts [2.47, 2.48]. For this aim, they have developed an effective force coarse-graining (CG) method, whereby atoms are grouped together to form several CG sites. In this way, MD simulations at a very large scale are possible. Figure 2.10 shows typical results of such calculations for the example of imidazolium nitrate [2.48]. Figure 2.10 (upper left) presents a snapshot of the tail groups of the alkyl chain with a length of four carbon atoms (C_4), whereas the upper right gives the corresponding snapshot for the anions. As can be seen, the ions are distributed relatively homogeneously, whereas the tail groups aggregate together and form several spatially heterogeneous domains. Increasing the alkyl chain length, this tail aggregation gets more pronounced, which

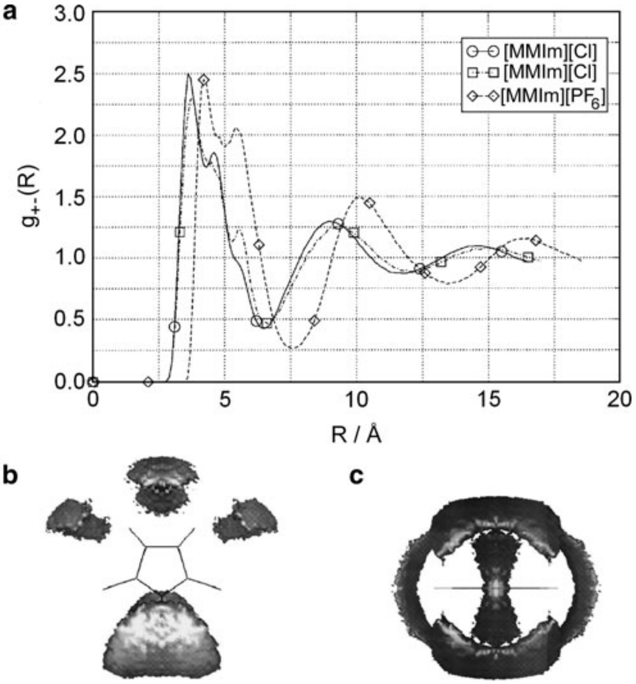

Fig. 2.9 (**a**) Pair distribution function $g_{+/-}(R)$ of liquid [MMIm][Cl] and [MMIm] [PF_6] at 400 K calculated with the united (*dashed line open circles* and *full line open diamonds*) and explicit (*full line squares*) atom model; (**b**) view from above of the 3D probability distribution of Cl^- ions around the $[MMIm]^+$ cation (united methyl model); (**c**) same as in (**b**), but viewed along the molecular symmetry down the C—H bond. Reprinted with permission from [2.46]; copyright permission (2010) by Taylor and Francis

is indicated by the pair distribution function in Fig. 2.10 (the lower left panel). In parallel, the diffusion of ions is clearly reduced with increasing tail aggregation; see Fig. 2.10 (lower right panel). On the basis of these results, it is concluded that for long enough side chains of the cations domain formation and liquid crystal-like structures should result. This is not restricted to imidazolium-based ionic liquids, but should occur in most organic ionic liquid systems [2.47].

The solubility and solvation of organic and inorganic compounds and of gases in ionic liquids is a crucial question, in both fundamental and applied research. Several of these aspects are treated in the book by Wasserscheid and Welton [2.13]. So, we may focus here on a few more recent theoretical investigations. Several groups have studied the solvation of imidazolium-based ionic liquids in mixtures with water, alcohols, acetronitrile, or DMSO [2.49–2.55]. The solvation of [C_2mim][Cl] in a cluster of 60 water molecules has been studied by Spickermann et al. with Car–Parrinello MD simulations. The authors could demonstrate that the structure of the hydration shell around the ion pair differs significantly from bulk water and that no ion pair dissociation occurs on the timescale of the simulation [2.50]. In MD simulations of 1-*n*-decyl-3-methylimidazolium bromide, [C_{10}mim][Br], in aqueous

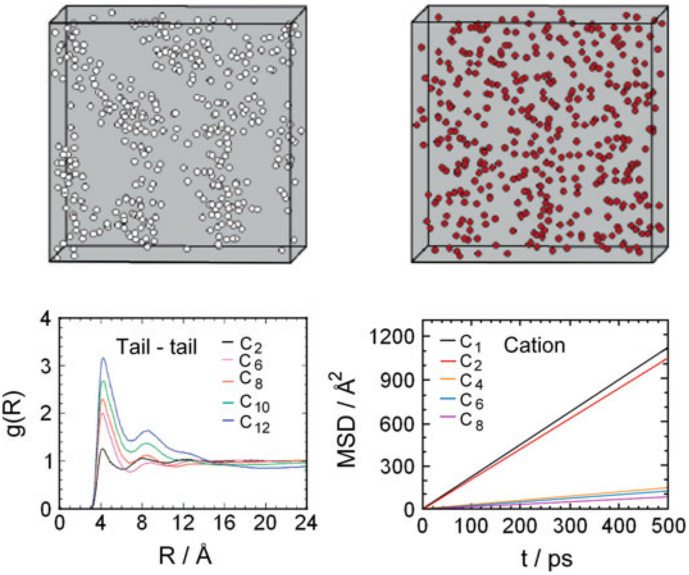

Fig. 2.10 Coarse-grained MD simulation of imidazolium nitrate with 400 ion pairs at $T = 700$ K: (*upper left*) snapshot of alkyl tail groups (alkyl chain length: C_4); (*upper right*) snapshot of anions only; (*lower left*) radial distribution function for tail–tail sites for different alkyl chain lengths C_i; (*lower right*) mean square displacements of cations. Reprinted with permission from [2.47]; copyright (2010) by American Chemical Society

solutions, it is found that cations spontaneously form small micellar aggregates where the decyl chains are buried inside the micelle and the polar head groups are exposed to water [2.49]. In their NMR and MD investigations of [C_4mim][Cl] in water and DMSO, Remsing et al. [2.53] find evidence of aggregation of butyl chains in aqueous environment. On the other hand, they show that [C_4mim][Cl] behaves as a typical electrolyte in water i.e. both ions are completely solvated at low concentrations. This seems to be not the case in DMSO [2.53]. The solvation of lanthanide cations (Ln = La, Eu, Yb) in imidazolium-based ionic liquids with different anions has been studied with MD simulations by Chaumont and Wipff [2.56, 2.57]. A main result of these studies is that in all cases the first solvation shell of Ln(III) is found to be purely anionic, with 6–8 coordinated ligands, and that this shell is surrounded by 13–14 [C_4mim]$^+$ cations leading to an *onion type* solvation of Ln(III).

As mentioned above, the experimental elucidation of the microscopic structure of room temperature ionic liquids employing diffraction methods is a complex problem and knowledge is rather limited. A review covering the literature up to 2006 has been written by Hardacre [2.58]. In general, a complete set of partial structure factors or distribution functions is not accessible. A specific complication in neutron scattering experiments is due to the large incoherent scattering cross section of hydrogen, which typically dominates the coherent contributions of other elements in the scattering function. In principle, this problem can be significantly reduced by deuterium isotope substitution. In X-ray diffraction, on the other hand, light elements such as hydrogen or deuterium are barely visible since the atomic form factors are proportional to the atomic number. So, the determination of the local structures in ionic liquids often requires further information, e.g. from the crystalline structures, MD simulations, or from NMR and Raman spectroscopy or EXAFS spectra. As an example of the experimental limitations, one may consider a recent study of Fujii et al. on the liquid structure of 1-ethyl-3-methylimidazolium bis-(trifluoromethylsulfonyl)imide, $[C_2mim][NTf_2]$ [2.59]. For the structural characterization, the authors have chosen X-ray measurements of the total scattering function, MD simulations of the conformers of $[C_2mim]^+$ and $[NTf_2]^-$, and NMR measurements of the ^1H, ^{13}C, and ^{19}F chemical shifts. Figure 2.11 presents the experimental total scatting intensity, $I(Q)$, in comparison with the contribution of intramolecular scatting calculated for a 1:1 mixture of the conformers. As can be seen, the intensity function at large $Q (Q > 4\,\text{Å}^{-1})$ solely reflects the intramolecular scattering. So all the information on the intermolecular structure at larger R is contained in the small section of $I(Q)$ at low $Q < 40\,\text{nm}^{-1}$. To resolve the structure from this part alone is not possible, i.e. independent results e.g. from MD simulations are needed. For the present example, the authors suggest the following model for the intermolecular structure: A nearest neighbour distance of 6 Å for the $[C_2mim]^+[NTf_2]^-$ correlation and a distance of 9 Å for the like ions correlation. From the NMR results, it is concluded that the C2 proton of $[C_2mim]^+$ strongly interacts with the O atom of the – $SO_2(CF_3)$ group of $[NTf_2]^-$ [2.59].

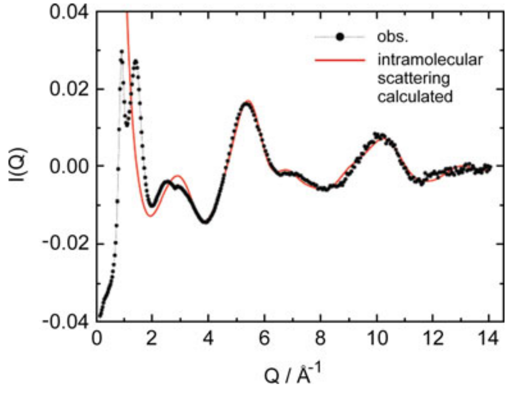

Fig. 2.11 X-ray scattering from liquid $[C_2mim]$ $[NTf_2]$ at 298 K: (*symbols*) total scattering intensity from X-ray measurement; (—) calculated intramolecular scattering contribution assuming a 1:1 mixture of $[C_2mim]$ and $[NTf_2]$ conformers. Reprinted with permission from [2.59]; copyright permission (2010) American Chemical Society

2.3 Bulk Phase Behaviour

Coulombic fluids span a wide range of temperatures extending from the low melting points of ionic liquids down to 200 K up to the critical temperatures of expanded fluid metals with that of tungsten being above 15,000 K. A representative collection of melting, boiling (decomposition temperatures in the case of ionic liquids) and critical temperatures is given in Table 2.2. Mainly for two reasons, the elements and compounds in this table have been chosen: First, they represent the typical range of melting points of the respective class of materials, and second, their thermophysical data are of interest in the following chapters.

The liquid range of a substance commonly is defined by the difference of the boiling and melting point temperatures. Accordingly, alkali metals and alkali halides have a high liquid range of the order of 600–700 K. Exceptionally high values of about 2,000 K are observed for Ga and W. In comparison with alkali halides, the liquid range of ionic liquids is rather reduced lying typically between 200

Table 2.2 Characteristic temperatures and thermodynamic data of Coulombic fluids: T_m = melting point, $T_\mathrm{b}(T_\mathrm{dec})$ = boiling point (decomposition temperature in the case of ionic liquids), T_c = critical temperature, ρ_m = liquid density at melting point, p_c = critical pressure

Coulombic fluids:	$\rho_m/\mathrm{g\,cm^{-3}}$	T_m/K	$T_b(T_{dec})/K$	T_c/K	p_c/bar
Metals					
Cs	1.84 (a)	301.8 (a)	963 (a)	1,924 (b)	92.5 (b)
Rb	1.47 (a)	312.1 (a)	975 (a)	2,017 (b)	124.5 (b)
K	0.83 (a)	336.4 (a)	1,031 (a)	2,198 (c)	155 (c)
Hg	13.54 (a)	234.3 (a)	629 (a)	1,751 (b)	1,673 (b)
Ga	6.04 (a)	302.9 (a)	2,217 (a)	–	–
Bi	9.99 (a)	544.5 (a)	1,391 (a)	–	–
W	19.26 (a) (at 298 K)	3,650 (a)	5,808 (a)	15,227 (h)	–
Molten salts					
KCl	1.52 (d)	1,045 (d)	1,680 (d)	3,200 (d)	~200 (d)
$BiCl_3$	3.92 (d)	505 (d)	714 (d)	1,178 (e)	~120 (d)
$AlCl_3$	2.48 (f)	465 (d) (at 2.5 bar)	453 (d) sublimes	626 (f)	26 (f)
Ionic liquids					
$[C_2mim][BF_4]$	1.26 (i)	288 (g)	$\lesssim$ 520	–	–
$[C_2mim]Cl$: $[AlCl_3]$(1:1)	1.29 (g) (at 298 K)	283 (g)	–	–	–
$[C_4mim][Cl]$	1.08 (g) (at 298 K)	338 (j)	$\lesssim$ 520	–	–
$[C_4mim][BF_4]$	1.14 (g) (at 298 K)	257 (g)	$\lesssim$ 630	–	–

Letters in brackets denote the following references: (a) = [2.60], (b) = [2.61], (c) = [2.62], (d) = [2.19], (e) = [2.63], (f) = [2.64],(g) = [2.13], h = [2.65], (i) = [2.66], (j) = [2.67] and 300 K, whereby the upper limit is determined by thermal decomposition. In principle, the liquid range of matter can be extended in two ways: By undercooling into a metastable state or by expanding the liquid at supercritical pressures up to the liquid–vapour critical region. For Coulombic fluids of interest, these variations shall be considered in detail here.

Most liquid metals can be undercooled below their melting point T_m; see e.g. [2.68]. For that purpose, it is necessary that the liquid is free of solid particles or intrinsic solid nuclei where the latter usually can be dissolved by heating the melt up to $\sim 1.2T_\mathrm{m}$ [2.68]. In large systems, undercooling is almost always limited by nucleation at extraneous interfaces. However, extreme levels of undercooling can be achieved by emulsification of liquid droplets ($\sim 10\,\mu$m radii) in an inert carrier fluid, which was reported for the first time by Turnbull [2.69]. Employing the droplet emulsion technique, Perepezko and coworkers have studied a number of liquid metals and alloys and have elucidated the effects of size and surface coating on undercooling [2.70–2.72]. For low melting point metals such as Ga and Bi, they found a lower limit of undercooling in the range of 0.3–$0.4T_\mathrm{m}$. The idea behind the dispersion technique is that the nucleation probability is strongly reduced because the catalytic effect of heterogeneous nucleants may be restricted to a small fraction of droplets. The technique is not limited to low melting metals, where carrier fluids such as alcoholic sodium oleate or silicon oils have been used, but can be extended to high melting point materials such as Ge if proper molten salts are employed as dispersion medium [2.73].

The second possibility to extend the liquid range of matter is that by expansion at elevated temperature and pressure. This is illustrated in Fig. 2.12 for the example of expanded fluid caesium [2.74]. The coexisting liquid and vapour densities up to the critical point and the density variation along different isobars between 60 and 200 bar are presented. It is worth to note that in the limits between the melting and critical point the coexisting liquid density expands by nearly a factor of 5 and that the temperature range from boiling to critical temperature, $T_\mathrm{c}/T_\mathrm{b}$, is extended by a factor of ~ 2. These two values are typical of fluid alkali metals; see also Table 2.2 and reference [2.61]. In the case of a molten salt such as $\mathrm{BiCl_3}$, the corresponding values are $\rho_\mathrm{m}/\rho_\mathrm{c} \sim 3$ and $T_\mathrm{c}/T_\mathrm{b} = 1.65$, which are comparable with those of typical molecular fluids; see e.g. [2.75]. Such a large expansion of fluids raises several fundamental questions: (1) Up to what density and temperature do the characteristic liquid properties such as the metallic or ionic conductance persist? (2) How do they transform to different states of condensed matter? These topics are discussed in detail in Chap. 3.

The bulk phase behaviour of molten salts and ionic liquids is dominated by Coulomb attraction between ions, which depends on the ion charges, the interionic distances and the coordination number, or the Madelung constant in the corresponding crystals. With this knowledge, some characteristic trends of the melting points are immediately understandable: For instance, the decrease in melting temperatures of the alkali halides with increasing anion or cation size. In particular, this explains the strong reduction of the melting points in room temperature ionic liquids due to the large size of the organic cations. Qualitatively, this also accounts

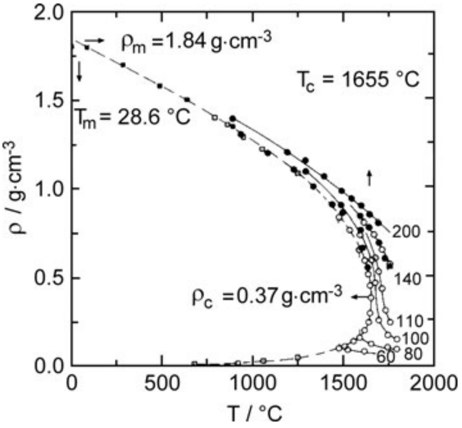

Fig. 2.12 Density variation of expanded fluid Cs at liquid–vapour coexistence and along different isobars between 60 and 200 bar at sub- and supercritical conditions. See also [2.74]

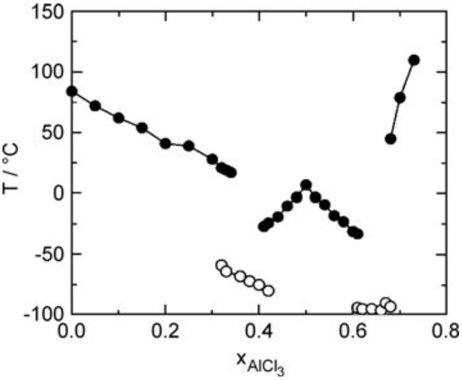

Fig. 2.13 Solid–liquid phase diagram for $[C_2mim]Cl{-}AlCl_3$ as a function of $AlCl_3$ mole fraction; *full symbols*, melting and freezing points, *open circles*, glass transition points. Adapted with permission from [2.16]; copyright permission (2010) by American Chemical Society

for the variation of the melting temperatures with changing the anion size, the trend being: $T_\mathrm{m}(\mathrm{Cl}^-) > T_\mathrm{m}(\mathrm{PF}_6^-) > T_\mathrm{m}(\mathrm{BF}_4^-) > T_\mathrm{m}(\mathrm{NTf}_2^-)$; see also [2.76]. A significant effect on the low temperature phase behaviour of ionic liquids is induced by varying the alkyl chain length C_n in e.g. $[C_n\mathrm{mim}]^+$ salts; see also [2.77]. Increasing the length from $n = 2$ to $n = 10$, the melting point is reduced with a trend for glass transition on cooling. For $n > 10$, the melting point increases again and liquid crystalline phases occur [2.13, 2.76]. The tendency to strong undercooling and low glass transition temperatures is especially pronounced in binary mixtures of imidazolium-based salts with $AlCl_3$ or with other Lewis acidic melts such as $ZnCl_2$ [2.16, 2.78]. This behaviour is similar to mixtures containing simple inorganic salts such as $KI + ZnCl_2$ [2.78]. An illustration is given in Fig. 2.13 for the phase diagram of $[C_2mim]Cl + AlCl_3$ [2.16].

Investigation of the high-temperature phase behaviour of ionic liquids is rather complicated due to thermal decomposition. The onset temperatures of decomposition are generally not well defined and reproducible. They depend on a number of influences such as impurities (especially water), wall reactions, and prolonged exposure at elevated temperatures; see also [2.13]. Therefore, the numbers in Table 2.2 may be considered as an average upper bound.

Near and slightly above the melting point, ionic liquids exhibit exceptionally low vapour pressures in their pure state ($<10^{-8}$ mbar according to the author's own experience with UHV experiments [2.79]), which for the first time enabled ultrahigh vacuum measurements such as XPS with a fluid system; see e.g. [2.80]. It is mainly this unusual property to which ionic liquids owe the name *green* solvents. Various attempts have been made to determine or estimate the thermodynamic properties, in particular, the vapour pressures, of different ionic liquids at elevated temperatures [2.81–2.84]. Rebelo et al. have tried to predict the boiling and critical point of a number of imidazolium-based ionic liquids on the basis of measured surface tension data and by extrapolation of the critical points with the use of the empirical Eötvös and Guggenheim relations. Such predictions have some severe uncertainties, not only because of the extrapolation over a wide temperature range, but also because it is not clear if these empirical laws apply to ionic liquids where charge ordering at the liquid/vapour interface should be considered – see also Sect. 2.5.2. Only recently, reliable measurements of the thermodynamic properties at elevated temperatures have been reported [2.83, 2.84]. By Knudsen effusion and transpiration measurements, Heintz and coworkers obtained the vapour pressure curves of $[C_2mim][NTf_2]$ and $[C_2mim][DCA]$ at temperatures up to 528 K and 480 K, respectively. They also could determine the gaseous enthalpy of formation of $[C_4mim][DCA]$ from combustion measurements and found good agreement with results from ab initio calculations. On the basis of these calculations, they conclude that the vapour phase is composed of ion pairs, i.e. $[C_4mim]^+[DCA]^-$, with a negligible degree of dissociation at the highest measured temperatures. This last result is supported by a recent mass spectroscopic study of several imidazolium-based salts. As for the nature of the vapour phase, these observations demonstrate the close similarity between ionic liquids and conventional molten salts. With the vapour pressure data of Heintz et al., finally, a more realistic extrapolation of two interesting quantities is possible: The vapour pressure near room temperature and the boiling point. For $[C_2mim][NTf_2]$ these are $p \sim 10^{-12}$ mbar, which is barely measurable, and $T_b \sim 1{,}200$ K, which is almost 600 K above the decomposition onset of this salt [2.85].

For a long time, criticality in Coulombic fluids has attracted the interest in theory and experiment alike; see e.g. [2.86–2.96]. Detailed knowledge of the thermodynamic properties near a liquid–vapour or liquid–liquid demixing critical point gives insight into the scaling behaviour and the nature of the dominant intermolecular interaction potential. In fluid alkali metals (Cs and Rb), Hensel and Warren [2.61] present a careful analysis of the coexisting liquid and vapour densities, ρ_l and ρ_v, and the diameter $\rho_d = (\rho_l + \rho_v)/2$ as a function of reduced temperature $\tau = (T_c - T)/T$ approaching the critical point up to $\tau \sim 10^{-3}$. From a single power law fit of $\Delta\rho/2\rho_c = (\rho_l - \rho_v)/2\rho_c$ vs. τ they find for the critical exponent β of the order parameter ρ a value of $\beta = 0.35$–0.36, which is close to the value of 0.325 predicted for the 3D Ising model. Therefore, these authors conclude that the critical behaviour of these fluid metals – despite the metal–nonmetal transition near the critical region, see Sect. 3.1 – can be described by short-range interactions, but it is not dominated by long-range Coulomb interactions. For binary liquid mixtures exhibiting a metal–nonmetal transition as a function of composition and a miscibility gap with an

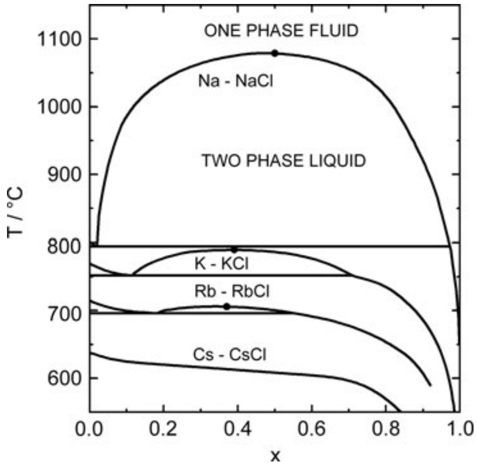

Fig. 2.14 High-temperature section of the phase diagrams – temperature T vs. metal mole fraction x – of alkali metal–alkali chloride melts; the *full dots* indicate the critical or consolute point of the respective system. See also [2.96]

upper critical point, differences in the critical behaviour have been reported. As an example of such systems, Fig. 2.14 shows the phase diagrams of alkali metal–alkali chloride melts.

Precise determinations of the liquid–liquid coexistence curve in Na-NH_3 solutions show a change of the critical exponent β from 0.502 to 0.34 at ~ 2 K below the consolute point [2.97]. Small-angle neutron scattering investigations of the concentration fluctuations in the critical region of $K - KBr$ melts indicate a behaviour corresponding to the 3D Ising model [2.98].

Research of the critical demixing of ionic liquid solutions at ambient conditions was started by Weingärtner and coworkers [2.99]. They studied systems of tetraalkylammonium salts dissolved in different aqueous and nonaqueous solvents, and also the system ethylammonium nitrate + n-octanol, which has an upper critical point of 315.2 K. From an experimental point of view, these systems are especially attractive for investigations of critical phenomena since the critical temperatures near ambient conditions allow temperature stabilization and control with a high precision. A systematic investigation of the coexistence curves of tetra-n-butylammonium picrate, N_{4444} Pic, solutions in 1- and 2-alkanols has been reported by Schröer, Weingärtner, and coworkers, whereby the dielectric constant at T_c varied from $\varepsilon = 16.8 - 3.6$ and the critical temperatures ranged from 315.87 to 351.09 K [2.100]. Figure 2.15 shows a typical example of the liquid–liquid miscibility gap in N_{4444} Pic in 1-tetradecanol. For the uncertainty of the critical temperatures, the authors give a value of ± 10 mK and that of the order parameter, the mass fraction w_c, is ± 0.004. From a detailed analysis of the scaling laws, the following conclusions are drawn. The critical exponent β for the coexistence curves lies near the Ising value, but shows systematic deviations with varying ε, from $\beta = 0.315$ at $\varepsilon = 16.8$ to $\beta = 0.36$ at $\varepsilon = 3.6$. For larger reduced temperatures $\tau > 0.01$ and using the mole fraction scale as order parameter, the critical exponent is near the mean field value of $\beta_{\text{eff}} = 0.5$. The authors do not draw a final conclusion on the problem of crossover to mean-field criticality, which is discussed in several of the earlier publications [2.95–2.97].

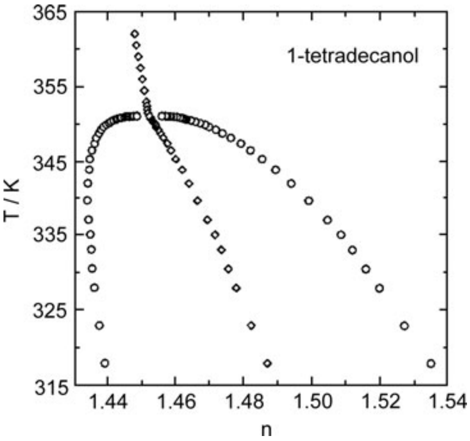

Fig. 2.15 Coexistence curve of solutions of N_{4444} Pic in 1-tetradecanol with an upper critical temperature of 351.09 K; plotted is the temperatures T vs. measured refractive index n as composition variable along the coexistence curve (*open circles*) and the coexistence curve diameter and an extension into the homogeneous liquid phase (*open diamonds*). Remarkable is the deviation of the diameter from the simple rectilinear diameter rule. Reprinted with permission from [2.100]; copyright permission (2010) from American Institute of Physics

Finally, assuming Ising criticality and the applicability of the rectilinear diameter rule, an empirical state behaviour of ionic liquid solutions seems possible, where all phase diagrams map on one master curve [2.101].

2.4 Transport Properties

Transport in fluid systems encompasses energy (thermal conductivity), momentum (viscosity) and particle transfer (diffusion) and, in Coulombic fluids, includes charge transfer characteristics (electrical conductivity). This is a broad field and, therefore, we content ourselves with a brief description of the electrical transport properties that are relevant to the discussion in later chapters and give reference to reviews for further details.

The theoretical basis of the electron transport in liquid metals is described in the monographs by Ziman [2.6] and Cusack [2.7]. Within the NFE model for metals, the DC conductivity is given by

$$\sigma(0) = n\,e\,\mu_\mathrm{e} = \frac{n\,e^2\tau_\mathrm{e}}{m_\mathrm{e}} = \frac{n\,e^2\lambda_\mathrm{e}}{m_\mathrm{e}v_\mathrm{F}}. \qquad (2.30)$$

Here, μ_e is the mobility, τ_e is the relaxation time, and λ_e is the mean free path of conduction electrons; the other symbols have their usual meaning, v_F being the Fermi velocity. For a calculation of τ_e, the scattering of conduction electrons by the pseudopotentials is treated as a weak perturbation and the positions of screened ions are taken into account by the structure factor $S(Q)$ of the liquid. This yields the Ziman formula for $\sigma(0)$ of liquid metals [2.6] as follows:

$$1/\sigma(0) = \frac{3\pi n}{e^2\hbar v_\mathrm{F}^2} \cdot \frac{1}{4k_\mathrm{F}^4} \int_0^{2k_\mathrm{F}} Q^2 S(Q)\phi(Q)^2 \mathrm{d}Q, \tag{2.31}$$

where $\phi(Q)$ is the Fourier transform of the pseudopotential. There are two further transport properties that within the NFE model are independent of τ_e: The Hall coefficient, R_H, which characterizes the electronic transport in a magnetic field vertical to the electric current, and the thermoelectric power, S, which is defined by the Thomson coefficient, σ_Γ, i.e. $S = \int_0^\Gamma (\sigma_\Gamma/T)\mathrm{d}T$. In the NFE model, these quantities are as follows:

$$R_\mathrm{H} = -(\mathrm{nec})^{-1}, \tag{2.32}$$

and

$$S = -\frac{\pi^2}{6} \cdot \frac{k_\mathrm{B}}{e} \left(\frac{k_\mathrm{B}T}{E_\mathrm{F}}\right) \tag{2.33}$$

Intuitively, one expects that the distance λ_e between two scattering events is large in comparison with the interatomic distance, which is of the order of $r_\mathrm{s} = (3/4\pi n)^{1/3}$ i.e. $\lambda_\mathrm{e} \gg r_\mathrm{s}$ – for alkali metals r_s is several Å. In this way, the conduction electrons can wander nearly freely through the metal and their wave functions can be approximated by plane waves. On the other hand, if the electrons were localized within an atomic distance, i.e. their uncertainty in position would be $\Delta x \sim r_\mathrm{s}$, then the uncertainty in momentum – since $k_\mathrm{F} \sim 1/r_\mathrm{s}$ – would be $\hbar k_\mathrm{F}$. Thus, a classical NFE model is impossible. The data in Table 2.3 give an overview how well the criterion $\lambda_\mathrm{e} \gg r_\mathrm{s}$ holds for liquid metals near their melting point.

Table 2.3 Experimental data of electronic DC conductivity, σ (0), electron mean free path, λ_e, Hall coefficient, R_H, divided by the NFE value according to (2.32), and conductivity ratio $\sigma/\sigma_\mathrm{calc}$; σ_calc has been determined according to (2.31) with pseudopotentials from phase shift analysis and with experimental $S(Q)$ data [2.102]

Metal	$\sigma/10^5\Omega^{-1}\mathrm{cm}^{-1}$	λ_e/Å	$R_\mathrm{H}/R_\mathrm{NFE}$	$\sigma/\sigma_\mathrm{calc}$
Na	1.04	157	0.98 (b)	1.77 (d)
K	0.77	176		2.1 (d)
Rb	0.45	118		1.2 (d)
Cs	0.27	82	1.0 (c)	1.1 (d)
Cu	0.47	34	1.0 (b)	
Al	0.41	18	1.0 (b)	
Ga	0.38	17	0.97...1.04 (b)	
Bi	0.078	4	0.7...0.95 (b)	

All data for liquid metals near the melting point; conductivities from (a) = [2.60]; (b) = [2.103], (c) = [2.104], (d) = [2.102]

In the liquid state, electronic conduction is not restricted to metals, but is also known to occur in mixtures with molten salts, possibly also in ionic liquids, although this has not been studied yet. In molten salts, two situations are of interest. At elevated temperatures salts such as the alkali or bismuth halides exhibit continuous miscibility with the respective metals and thus, as a function of added metal, undergo a nonmetal–metal transition. In this context, one of the fundamental questions is, what is the electronic structure in the nonmetallic salt-rich melts and how does it change towards the metal-rich solutions? With these problems, we will be concerned in Sect. 3.5. Another important mechanism of electron conduction in molten salts prevails in systems that contain two valence states of the same metal element. Typical examples are mixtures of $NdI_2 - NdI_3$ [2.105–2.107], $CuCl - CuCl_2$ [2.108], or solutions of transition metal halides such as $TaCl_5$ or $NbCl_5$ in molten salts such as NaCl or CsCl [2.109]. The composition in these mixtures can be varied by changing the ratio of the salt components of different valency, by adding metal to the salt of higher valency, or, in electrochemical experiments, by changing the applied electrochemical potential in an electrochemical cell with a solution of e.g. $TaCl_5 - NaCl$ [2.109]. The electronic transport in these systems is thermally activated, which can be explained by intervalence charge transfer in a simple two-site model [2.107, 2.109]. As a function of composition, the electronic conductivity exhibits a parabolic dependence with a clear maximum, whereby the conductivities at the maximum range from $\sim 10^{-2}\,\Omega^{-1}\,\mathrm{cm}^{-1}$ [Ta(IV) – Ta(V) in CsCl – NaCl] to $10\,\Omega^{-1}\,\mathrm{cm}^{-1}$ ($CuCl - CuCl_2$ at a temperature near 1,000 K); see Fig 2.16. The parabolic concentration dependence is easy to understand if one takes into consideration that for a successful intervalence charge transfer two ions of different valency have to be nearest neighbours; the probability for this is proportional to the product of the respective mole fractions, e.g. $x(\mathrm{Ta\,IV}) \cdot x(\mathrm{Ta\,V})$. In applications, where optimization of current efficiencies matters, knowledge of the electronic conduction component is very valuable.

The ionic DC conductivity in molten salts and ionic liquids can be described by the following equation:

$$\sigma_{\mathrm{ion}}(0) = \sum_i n_i q_i \mu_i , \qquad (2.34)$$

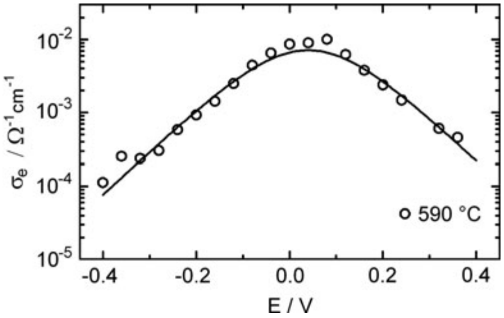

Fig. 2.16 Impedance measurements of the electronic DC conductivity vs. electrochemical potential *E* in a $CsCl - NaCl$ – 3 mol% Ta (IV, V) oxychloride melt at 863 K; (*open circles*) experimental points; (*full line*) fit with a parabolic function. See also [2.109]

where n_i is the number density, q_i the charge, and μ_i the mobility of ions $i\,(i = +, -)$. The mobility is given by the Einstein relation,

$$\mu_i = \frac{D_i q_i}{k_\mathrm{B} T}, \tag{2.35}$$

where D_i is the self-diffusion coefficient of ion i. Thus, the ionic conductivity is directly related with the self-diffusivity of the ions; the molar conductivity, $\Lambda = \sigma/c$, is then determined by

$$\Lambda = \left(\frac{F^2}{RT}\right)(D_+ + D_-). \tag{2.36}$$

Here, F is the Faraday constant, R is the gas constant, and c is the molar concentration. Conductivities calculated from (2.36) with independently measured ion diffusion coefficients may deviate from measured ionic conductivities. Both in molten salts [2.110] and in ionic liquids [2.111, 2.112], these deviations are explained by short-lived ion pairs. These pairs can contribute to diffusion, but not to the electrical conductance. Via the Stokes–Einstein relation, there is a strong coupling between the viscosity, η, and the diffusion, and thus between viscosity and ionic conductivity. So, in many cases, the temperature dependence of the ionic conductivity follows a Vogel–Tammann–Fulcher (VTF) relation,

$$\sigma_\mathrm{ion}(T) = \sigma_0 \exp\left(\frac{-B}{(T - T_0)}\right) \tag{2.37}$$

and correspondingly for η, which is inversely proportional to σ_ion. In (2.37), B is referred to as a pseudo-activation energy and T_0 is the zero-mobility temperature or glass transition temperature. Typical values of conductivities, viscosities, and self-diffusion coefficients of a few ionic liquids in comparison with molten salts are given in Table 2.4.

Table 2.4 Ionic DC conductivity σ_ion, diffusion coefficients D_+ and D_-, and viscosity η, of selected molten salts and ionic liquids

Ionic melt	T_m/K	$\sigma_\mathrm{ion}/\Omega^{-1}\mathrm{cm}^{-1}$	$D_+/10^{-7}\,\mathrm{cm}^2\mathrm{s}^{-1}$	$D_-/10^{-7}\mathrm{cm}^2\mathrm{s}^{-1}$	η/c Poise
NaCl	1,081	3.61	962	673	1.43
KCl	1,045	2.2	–	–	1.34
CsCl	918	1.09	350	380	1.60
$BiCl_3$	505	0.38	–	–	42.2
$ZnCl_2$	556	0.02	–	–	18,000
[C_2mim][BF_4]	288 (b)	0.14 (c)	5.0 (d)	4.0 (d)	35(c)/43 (c)
[C_2mim][NTf_2]	258 (b)	0.008 (c)	5.0 (d)	3.0 (d)	33 (b)
[C_4mim][BF_4]	192 (c)	0.005	1.8 (c)	1.8 (c)	75 (c)

Data of molten salts are from reference (a) at conditions near their respective melting points, those of ionic liquids correspond to 298 K and, for σ_ion, to 303 K; (a) = [2.19], (b) = [2.111], (c) = [2.67], (d) = [2.112]

With regard to these data, it is striking that the conductivities of molten salts near their melting points are of the same order of magnitude, $\sim 1\,\Omega^{-1}\,\mathrm{cm}^{-1}$. Exceptions are melts such as $ZnCl_2$, which are characterized by a network structure (see Sect. 2.2.2) and so are not completely dissociated molten salts. On comparing the conductivities and diffusion coefficients of the high-temperature molten salts with those of room temperature ionic liquids, they differ by roughly two orders of magnitude. However, if one extrapolates the values of ionic liquids to high temperatures near 1,000 K with the aid of (2.37) – for instance, for $[C_2mim][BF_4]$ B is $\sim$720 K and $T_0 \sim 150\,\mathrm{K}$ [2.112] – these hypothetical conductivities and diffusivities would be comparable with the values of molten salts. So, the essential difference between both classes of ionic media is less in their transport properties, but in their thermal stability and, of course, in the large chemical variability of ionic liquids.

2.5 Interfacial Characteristics

The behaviour of fluids at surfaces[2] and interfaces is a classical area of physical chemistry. It includes a variety of topics such as surface thermodynamics, adsorption phenomena, catalysis, tribology, micro- and nanofluidics, or processes at electrified liquid/solid interfaces; to name some of the most important subjects; see also [2.113]. Phenomena at fluid interfaces are not only of fundamental interest, but also of great practical importance in different fields. In many respects, surface science is also the basis for nanoscience and technology, since nano-objects – for which the number of atoms on the surface and in the interior are of comparable magnitude – are strongly determined by their surface characteristics and by interfacial phenomena. In recent years, research of fluid interfaces has made considerable progress based on new developments of microscopic theories and experimental techniques. For instance, with X-ray reflectivity measurements at high flux synchrotron sources and scanning probe microscopy, two powerful tools became available to probe the microscopic structure of surfaces and interfaces. In consequence, novel interfacial phenomena such as wetting and prewetting transitions, surface melting and freezing, or electrochemical nanostructuring have attracted special interest in physics, chemistry, and material science. With respect to liquid metals and molten salts or ionic liquids, studies of these topics at elevated temperatures are also of special practical interest. This covers applications in soldering, metal–metal or metal–ceramic bonding, and liquid metal embrittlement – see e.g. [2.114] – and also problems of thin film stability in integrated circuits or electrochemical 2D and 3D phase formation and growth. Some of these interfacial phase transitions of Coulombic fluids, at the liquid/vapour, the liquid/solid, and the electrified liquid/solid electrode interfaces, are dealt with detail in Chaps. 4 and 5. In the following, some basic characteristics are introduced from a more phenomenological point of view.

---

[2] The term surface often is used for interfaces where one of the neighbouring phases is a vapour phase or vacuum.

2.5.1 Liquid Metals

Across the liquid/vapour interface, metals exhibit a singular variation of their electronic structure: They undergo a metal–nonmetal (M − NM) transition and so, at temperatures well below the critical one, the character of the interatomic interaction changes abruptly from screened Coulomb interaction in the liquid to a Lennard–Jones type potential in the insulating vapour phase. The effect of this electronic transition on the microscopic structure of a liquid metal surface was first studied by Rice and coworkers [2.115]. Their Monte Carlo simulations of the inhomogeneous interfacial region indicated that the liquid/vapour interface of metals is stratified, i.e. a layered structure exists at the interface that decays over several atomic diameters into the bulk liquid. Experimental evidence of this stratification was obtained by X-ray reflectivity measurements on different liquid metals [2.116–2.118]. Figure 2.17 shows a comparison of theoretical with experimental results of the density distribution normal to the liquid/vapour interface of Ga at conditions near the normal melting point. The calculations are based on self-consistent quantum Monte Carlo simulations with pseudopotential representation of the electron–ion and ion–ion interactions [2.119], the experimental curve results from X-ray reflectivity measurements [2.117]. It is interesting to add that at the solid/vacuum interface of metals the electron distribution exhibits a similar oscillatory behaviour decaying into the bulk after several atomic layers; see e.g. [2.120].

For a description of the macroscopic interfacial properties, the Gibbs adsorption equation is fundamental. We consider a multicomponent system with two bulk phases, α and β, in equilibrium and separated by a plane located near a planar interface. Then the Gibbs equation is [2.113] as follows:

$$\mathrm{d}\sigma_{\alpha\beta} = -S^{(\sigma)}\mathrm{d}T - \sum_i \Gamma_i^{(\sigma)}\mathrm{d}\mu_i. \tag{2.38}$$

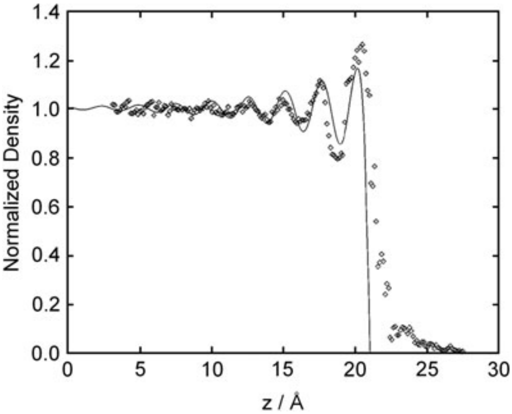

Fig. 2.17 Normalized density distribution along the normal to the liquid/vapour interface of Ga near its melting point; (*open diamonds*) from quantum Monte Carlo simulations; (*full line*) from X-ray reflectivity measurements. Adapted with permission from [2.119]; copyright permission (2010) by American Physical Society

It relates the interfacial free energy per unit area, $\sigma_{\alpha\beta}$ – which is numerically equal to the surface tension – to the relative interfacial entropy per unit area, $S^{(\sigma)}$, and the relative adsorption or interfacial excess per unit area, ${\Gamma_i}^{(\sigma)} = {n_i}^{(\sigma)}/A$, with A being the area of the interface, T the temperature, and μ_i the chemical potential of component i. The mole number is ${n_i}^{(\sigma)} = n_i - {n_i}^{\alpha} - {n_i}^{\beta}$. Since the ${\Gamma_i}^{(\sigma)}$ are defined relative to an arbitrarily chosen Gibbs dividing surface, the surface can be placed such that one ${\Gamma_j}^{(\sigma)} = 0$. For a binary system of solvent 1 and solute 2, one can choose ${\Gamma_1}^{(\sigma)} = 0$, so that at constant temperature the interfacial excess of 2 relative to 1 is $\Gamma_{2(1)}^{(\sigma)} = -(\partial\sigma_{\alpha\beta}/\partial\mu_2)_T$. If the slope of $\sigma_{\alpha\beta}$ vs. μ_2 is negative, then there is an actual excess or enrichment of solute at the interface. In the opposite case, there is a deficiency of solute. In the case of solid/vapour interfaces, $\sigma_{\alpha\beta}$ is not generally equal to the surface tension because of crystallographic anisotropy and of changes in the state of surface stress on increasing the surface area. However, at temperatures near the melting point, these effects are reduced due to the relatively high atomic mobility. Similar considerations apply if a solid α is in contact with its own liquid – for instance, at nucleation in supercooled melts – or with a second solid having a negligible solubility in α.

Representative values of the interfacial free energies of pure metals are listed in Table 2.5 for the liquid/vapour, the solid/vapour, and the solid/liquid interface at conditions near the respective melting points. Also given are the temperature coefficients, $-\partial\sigma_{\mathrm{lv}}/\partial T = S^{(\sigma)}$.

A careful analysis of the σ_{lv} data from the literature obtained by different methods has been performed by Allen [2.121], who suggests the following reliability limits: ±5% for the surface tensions σ_{lv} and ±50% for the temperature coefficients. Several attempts have been made to correlate the surface tension of liquid metals with bulk thermodynamic properties. Qualitatively, the data in Table 2.5 suggest that σ_{lv} increases with the melting temperature T_{m}, Ga being an exception. A quantitative fit of most experimental data is obtained by the empirical relation: $\sigma_{\mathrm{lv}} = 3.6\,T_{\mathrm{m}} \cdot {V_{\mathrm{m}}}^{-2/3}$, where V_{m} is the molar volume of the liquid and the prefactor has the dimension $10^{-7}\,\mathrm{J\,K^{-1}}$ [2.121]. This correlation is consistent with the temperature dependence of σ_{lv} of liquid metals that follow the simple Eötvös law: $\sigma_{\mathrm{lv}} = k_{\mathrm{E}}(T_{\mathrm{c}} - T){V_{\mathrm{m}}}^{-2/3}$, with $k_{\mathrm{E}} \sim 0.64 \times 10^{-7}\,\mathrm{J\,K^{-1}}$ and $T_{\mathrm{c}} \sim 6.6\,T_{\mathrm{m}}$.

Table 2.5 Representative selection of surface free energies, $\sigma_{\alpha\beta}$, of metals at the liquid/vapour (l/v), solid/vapour (s/v), and solid/liquid (s/l) interface at conditions near the melting point; the σ_{sv} – data correspond to polycrystalline surfaces

Metal	$\sigma_{\mathrm{lv}}/\mathrm{mJ\,m^{-2}}$	$\sigma_{\mathrm{sv}}/\mathrm{mJ\,m^{-2}}$	$\sigma_{\mathrm{sl}}/\mathrm{mJ\,m^{-2}}$	$\partial\sigma_{\mathrm{lv}}/\partial T/\mathrm{mJ\,m^{-2}\,K^{-1}}$
K	115 ± 10 (a)	–	–	−0.08 (a)
Ga	730 ± 10 (b)	767 ± 6 (c)	82 (d)	−0.09 (b)
Bi	375 ± 10 (b)	501 ± 4 (c)	99 (d)	−0.11 (b)
Au	1,140 ± 50 (a)	1,410 ± 30 (c)	128 (d)	−0.5 (a)
Fe	1,900 ± 100 (a)	2,170 (c) γ-Fe	269 (d)	−0.5 (a)
W	2,500 ± 150 (a)	2,690 ± 22 (c)	436 (d)	−0.3 (a)

(a) = [2.121], (b) = [2.122], (c) = [2.123], (d) = [2.124]

With these data, the above prefactor results. Further correlations that take into account the atomic bond strengths by the corresponding enthalpies of phase transition and consider the number of broken bonds at the interface have been tested. This yields the relation: $\sigma_{\mathrm{lv}}\,(T_{\mathrm{m}}) = 0.174 \times 10^{-8}\mathrm{mol}^{1/3}\Delta H_{\mathrm{V}} V_{\mathrm{m}}^{-2/3}$, where ΔH_{V} is the molar enthalpy of evaporation at T_{m}. It gives a very god fit of experimental σ_{lv} data with a correlation coefficient of 0.998 [2.125]. On the same basis of a broken bond model, a relation has been derived between σ_{sv} and σ_{lv} of the form [2.115]: $\sigma_{\mathrm{sv}} = (Z - Z^{(\sigma)})/\Delta H_{\mathrm{f}} V_{\mathrm{m,s}}^{-2/3} + (\rho_{\mathrm{s}}/\rho_{\mathrm{l}})^{2/3}\sigma_{\mathrm{lv}}$; here, Z denotes the coordination number in the bulk solid, $Z^{(\sigma)}$ that at the surface, ΔH_{f} is the molar heat of fusion, $V_{\mathrm{m,s}}$ is now the molar volume of the solid, and ρ_{s} and ρ_{l} are the solid and liquid density, respectively, at T_{m}. The main simplifying assumption is that the bond energies of surface and bulk atoms are equal. Depending on the packing of atoms in the surface planes – corresponding to hcp, bcc, and fcc crystal structures – lower and upper bounds for the ratio $\sigma_{\mathrm{sv}}/\sigma_{\mathrm{lv}}$ can be estimated from the above relation [2.121]: $1.1 \precsim \sigma_{\mathrm{sv}}/\sigma_{\mathrm{lv}} \precsim 1.3$. Thus, an anisotropy of about 20% is estimated for the surface tension of crystalline metals. Theoretical determinations of the surface tension anisotropy in transition metals yield the following results [2.126]: For fcc crystals such as Ni cleaved with different surface orientations, it is found that $\sigma_{\mathrm{sv}}(110) > \sigma_{\mathrm{sv}}(110) > \sigma_{\mathrm{sv}}(111)$ with $\sigma_{\mathrm{sv}}(110)/\sigma_{\mathrm{sv}}(111) = 1.3$; likewise, for bcc crystals with half band filling the corresponding inequality is $\sigma_{\mathrm{sv}}(100) > \sigma_{\mathrm{sv}}(111) > \sigma_{\mathrm{sv}}(110)$ with $\sigma_{\mathrm{sv}}(100)/\sigma_{\mathrm{sv}}(110) = 1.4$. In both cases, a relatively strong anisotropy is predicted. Experimental values for different noble and transition metals amount to $\sim$10% [2.121]. The data given in Table 2.5 for the solid/liquid interfacial free energies σ_{sl} have been determined from homogeneous nucleation rates in strongly undercooled liquid metals and are compiled in [2.124]. For metals, Turnbull found the following rule: $\sigma_{\mathrm{sl}}(T_{\mathrm{m}}) = 0.45\,\Delta H_{\mathrm{f}}\,V_{\mathrm{m,s}}^{-2/3}$ [2.127], which has been verified on simple thermodynamic grounds [2.128].

Wetting phenomena of liquid metals are of particular interest in various metallurgical applications such as soldering, brazing, and welding and in problems with heat transfer or floatation. Wetting, generally, describes the spreading of a liquid deposited on a solid or liquid substrate. In order to simplify, consider a liquid drop on top of a clean, smooth, non-deformable, and horizontal solid surface. Then, three configurations are of particular interest, which can be distinguished by the magnitude of the contact angle Θ – this is defined by the angle between the solid surface and the tangent to the liquid surface at a point on the three phase contact line, taken in a plane vertical to the solid surface. The three distinct wetting configurations are as follows: (1) non-wetting for $\Theta > 90°$; (2) partial wetting for $0 < \Theta \leq 90°$; and (3) complete wetting in the limit $\Theta = 0$. The contact angle depends on the surface free energies of the three phases in contact: Solid (s), liquid (l), and vapour (v). At three-phase equilibrium, the total surface free energy, $\Delta F^{(\sigma)}$, has a minimum, $\partial\Delta F^{(\sigma)}/\partial A = 0$ from which the Young equation follows (see also [2.113]):

$$\sigma_{\mathrm{lv}} \cos\Theta = \sigma_{\mathrm{sv}}^{0} - \sigma_{\mathrm{sl}}. \tag{2.39}$$

It is important to note that the three phases are in mutual equilibrium and so the solid surface must be in equilibrium with the saturated vapour at pressure p_0. Consequently, there must be an adsorbed film with a film pressure π_0, i.e. $\sigma^0_{\mathrm{sv}} = \sigma_{\mathrm{sv}} - \pi_0$, where σ_{sv} is the surface free energy of the pure solid substrate. In the limiting case $\Theta = 0$, (2.39) does not hold any longer and $\Theta = 0$ is not defined. This situation corresponds to the condition of a wetting transition.

Further insight into the distinct wetting configurations may be obtained by the spreading coefficient S, which is defined by

$$S = \sigma^0_{\mathrm{sv}} - (\sigma_{\mathrm{lv}} + \sigma_{\mathrm{sl}}). \tag{2.40}$$

It measures the difference between the surface free energy of the substrate when *dry and wet*. If $S > 0$, the liquid spreads completely and thus lowers the surface free energy. The opposite case, $S < 0$, corresponds to partial or non-wetting. Very similar considerations hold for spreading of a liquid over another liquid [2.113].

Research on wetting phenomena during the last decades was stimulated by a seminal paper of J. W. Cahn on *Critical point wetting* [2.129]. He could show *that in any two phase mixture of fluids near their critical point, contact angles against any third phase become zero in that one of the critical phases completely wets the third phase and excludes contact with the other critical phase…At some temperature below the critical, this perfect wetting terminates in what is described as a first-order transition of the surface*. The situation is illustrated in Fig. 2.18, which shows the phase diagram of a binary fluid mixture of components A and B exhibiting a miscibility gap. This is defined by the coexistence curve of phases α and β with an upper critical temperature T_{c}. In order to describe the characteristic wetting transitions in this system, let us focus on two specific variations of the thermodynamic states indicated by paths (1) and (2) in the figure. If at coexistence along path (1) the surface excess $\Gamma_A(\Gamma_B \equiv 0)$ has a low and finite value, but diverges at some temperature T_{w}, this is the signature of a first-order, critical wetting transition, with T_{w} being the wetting temperature. Connected with this first-order wetting transition are so-called prewetting transitions, where a discontinuous jump from microscopically thin to thick adsorption films occurs and which can be observed off of coexistence along path (2) in the homogeneous B-rich fluid phase. The loci of these prewetting transitions define the prewetting line that leaves the coexistence curve tangentially at T_{w} and ends in a critical prewetting point at T_{cpw} – see the dashed line in Fig. 2.18. Along path (2) the distance to the coexistence curve is measured by the difference in the chemical potential, $\Delta\mu$, relative to μ_0 at coexistence. Following $\Gamma_A(\Delta\mu)$ along path (2) all the way to two phase coexistence, the surface excess continuously increases and diverges at coexistence. This is denoted a complete wetting transition. So, for $T_{\mathrm{w}} < T < T_{\mathrm{c}}$ along the coexistence curve, a macroscopically thick wetting film of the A-rich phase α separates the β phase from the vapour phase – or the container wall with T'_{w}. For an in depth presentation and discussion of the theory of wetting transitions, reference is given to the review article by Dietrich [2.131]. Wetting phenomena in nanofluidics have been treated recently in a review by Rauscher and Dietrich [2.132]. A very recent review on

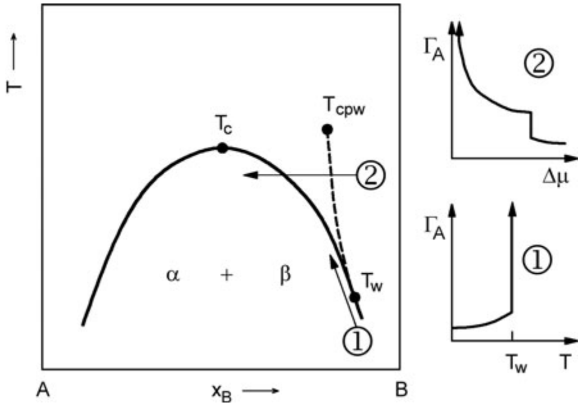

Fig. 2.18 Schematic bulk phase diagram of a binary fluid mixture exhibiting a miscibility gap, which is defined by the coexistence curve of phases α and β with an upper critical temperature T_c (*full line* in the temperature–mole fraction plane). Included in this figure is the surface phase diagram with a critical wetting transition at T_w and prewetting transitions along the prewetting line (*dashed line*). Changes in the surface excess Γ_A accompanying the distinct wetting transitions along paths (1) and (2) are depicted in the figures to the right. See also [2.130]

wetting and spreading covering various fundamental aspects and applications, with a high number of nearly 600 references, is that by Bonn et al. [2.133].

2.5.2 Molten Salts and Ionic Liquids

Various theoretical investigations have focused on the interfacial structure of molten salts. Evans and coworkers have calculated the equilibrium density profile and surface tension for the liquid/vapour interface within the restricted primitive model of a molten alkali halide. In this model, the anions and cations are represented by hard spheres of equal diameter and opposite charges. Using a square gradient approximation to calculate the free energy of the inhomogeneous charged fluid, they find differences in the shape of the density profile in comparison with a Lennard–Jones fluid, in particular, a sharper thickness of $\sim R$ – R being the radius of hard spheres – near the melting temperature. The theory gives a reasonable description of both the magnitude and the temperature dependence of surface tensions of alkali halides and other salts of nearly equal ionic radii [2.134, 2.135]. A number of molecular dynamics simulations of solid and liquid interfaces of salts have been performed by Heyes et al. [2.136, 2.137]. Of particular interest are the results obtained for a liquid/rigid wall and the corresponding electrified interface. A Born–Mayer–Huggins potential was used to model the ionic interactions with parameters for KCl [2.136]. It is found that close to and in a direction perpendicular to the wall there is substantial structural ordering. Oscillations in the density profile indicate a tendency towards layering of the ions near the liquid/wall interface; these oscillations die away rapidly towards

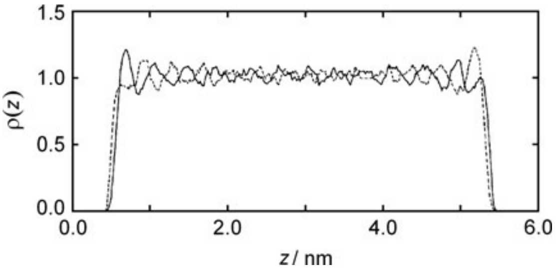

Fig. 2.19 MD simulation of the ion density profile, $\rho(z)$, vertical to the electrified liquid/wall interface of KCl at 1,075 K; (*full line*) corresponds to K^+, (*dashed line*) to Cl^-; densities are relative to the bulk liquid value. The formation of alternating K^+- and Cl^--rich layers is apparent. Adapted with permission from [2.136]; reproduced by permission (2010) of The Royal Society of Chemistry

the bulk. Similar effects are known from MD calculations of hard-sphere fluids against a repulsive wall and are predicted by theory; see e.g. [2.138]. Applying an electric field of $\sim 10^9$ V m^{-1} perpendicular to the liquid KCl/wall (electrode) interface, evidence is found of charge separation and ordering, whereby the oscillations of charge densities now penetrate much further into the bulk – see also Fig. 2.19. In relation to the double layer problem of electrified interfaces of ionic fluids, these findings are of special importance. Finally, it must be noted that experimental investigations of the microscopic structure of the liquid/vapour interface of molten salts such as alkali halides are still missing. Such experiments are complicated due to the fact that alkali halides have a relatively high vapour pressure near their melting point, which makes the use of ultrahigh vacuum techniques difficult.

Most metals – and other solid systems such as rare gases or ice – exhibit the phenomenon of surface melting approaching the melting point from below T_{m} during which the solid is wet by its own liquid – see e.g. [2.139]. It seems that this is not the case in salts such as the alkali halides. Indications of partial wetting connected with a contact angle of ~48° have been observed in an experiment of an Ar bubble captured at a crystalline NaCl/melt interface [2.140]. In a recent theoretical study, this problem of incomplete wetting of alkali halide crystal surfaces by their own melt at the triple point has been tackled by Tosatti and coworkers [2.141]. Using classic Born–Mayer–Huggins–Fumi–Tosi two-body potentials, these authors have performed extensive simulations for NaCl and have calculated the solid/liquid, liquid/vapour and solid/vapour interfacial free energies. They could show that NaCl(100) is a nonmelting surface with $\sigma_{\mathrm{sv}} < \sigma_{\mathrm{sl}} + \sigma_{\mathrm{lv}}$. This behaviour is explained by mainly three factors (1) Surface anharmonicities stabilize the solid surface and thus reduce σ_{sv}; (2) A large density jump on melting causes bad liquid – solid adhesion; (3) Incipient NaCl molecular correlations at the liquid/vapour interface lead to a reduction of the surface entropy of liquid NaCl below that of solid NaCl(100) and thus raise σ_{lv}. These are interesting predictions, waiting for an independent experimental confirmation.

The structure and composition of liquid/vapour or liquid/vacuum interfaces of room temperature ionic liquids have been studied quite intensively in recent years. In a first atomistic simulation of dimethylimidazolium chloride, Lynden-Bell found indications of charge ordering and a region of enhanced density immediately below the interface in which the cations are oriented with their planes perpendicular to the surface [2.142]. Similar conclusions were drawn from a more recent MD simulation study of [C_4mim][PF_6] melts, where the butyl chains are observed to project outside the liquid surface and the imidazolium ring plane is found to lie parallel to the surface normal [2.143]. These findings have been supported by direct recoil spectroscopy measurements [2.144] and also by sum frequency generation (SFG) spectroscopy [2.145]. Seemingly conflicting propositions were derived from X-ray reflectivity measurements where it was claimed that these data are not consistent with a model in which the butyl chains protrude from the air/liquid interface [2.146]. However, this conflict could be solved unambiguously by a combined SFG and X-ray reflectivity study of imidazolium-based ionic liquids with different anions such as BF_4^-, PF_6^-, and I^- by Jeon et al. [2.147]. From a careful analysis of their reflectivity data in conjunction with the SFG spectra, these authors give evidence that the gas/liquid interface of these melts consists of a topmost layer of loosely packed butyl chains, while the densely packed imidazolium cores and anions form a layer in contact with the bulk liquid. Furthermore, the surface composition of various 1,3-dialkyl-imidazolium ionic liquids was studied by X-ray photoelectron spectroscopy [2.80]. Again, a clear enrichment of the alkyl chains at the outer surface is found; it is further concluded that both anions and cationic head groups are located approximately at the same distance from the outer surface [2.80].

It is known for a long time that charged walls in contact with an electrolyte solution strongly affect the interfacial structures and properties. This was first demonstrated by Langmuir in explaining the capillary rise of a dilute KCl solution in a quartz or glass tubing [2.148]. This effect can also explain a strong enhancement of the wetting film thickness at the molten KCl/sapphire interface due to charging of Al_2O_3 and double layer formation at the interface [2.149]; see also Sect. 4.3. The microscopic structure of an ionic liquid/charged wall interface has been elucidated, for the first time experimentally, for an ionic liquid at a charged sapphire (0001) surface [2.150]. This interface was probed by high energy X-ray reflectivity measurements spanning a momentum transfer range up to $q = 1.4\,\text{Å}^{-1}$. In a temperature range from -15°C up to 110°C, three ionic liquids with different cations and the common $[FAP]^-$ anion have been studied, where $[FAP]^-$ stands for bis(pentafluoroethyl)trifluorophosphate. Charging of the Al_2O_3 surface was independently measured with a Kelvin probe. One of the main observations is that all reflectivity curves in the temperature range studied show a clear dip around $q_0 \sim 0.8\ \text{Å}^{-1}$. This is a strong indication of interfacial layering with a layer spacing of $d = 2\pi/q_0 \sim 8\text{Å}$ comparable in size with the thickness of an anion–cation double layer. A detailed analysis of the Fresnel-normalized reflectivity curves by fits with different models of the interfacial electron density profiles yields a layering structure of alternating cation and anion strata, which decays exponentially into the bulk with a decay length of $\sim$16 Å at the lowest temperature; see Fig. 2.20. In

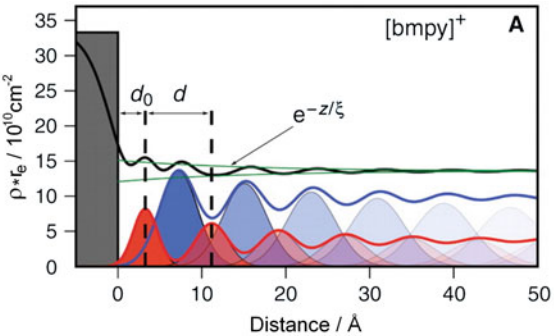

Fig. 2.20 Molecular layering in a fluorinated ionic liquid at a charged sapphire (0001) surface: Electron densities obtained from the best fit of the X-ray reflectivity measurement for the [C_4mpy] [FAP]–Al_2O_3 interface at −15°C; red and blue lines indicate cation and anion Gaussian distributions contributing to the respective partial electron density profiles; *black line*, total electron density profile, *grey bar*, electron density of sapphire substrate without roughness. From [2.150], reprinted with permission from the American Association for the Advancement of Science (2010)

conclusion, there is a close similarity in charge ordering at an electrified solid/liquid interface between an ionic liquid and a molten salt such as KCl; see Fig. 2.19.

Electrocapillarity and electrowetting phenomena have attracted considerable interest in recent years; see e.g. the review by Mugele and Baret [2.151]. Strong motivations result from potential applications in *lab-on-a chip* devices or new kinds of electronic displays. Electrowetting enables the manipulation of tiny amounts of liquids on surfaces. The basic equation behind this is the Young–Lippmann equation; see [2.151]:

$$\cos\Theta = \cos\Theta_0 + \left(\frac{C}{2\sigma_{\mathrm{lv}}}\right) \cdot U^2, \tag{2.41}$$

which describes the variation of the contact angle Θ of a liquid droplet of a conducting fluid on top of a thin dielectric film with capacitance C as a function of voltage U applied across the droplet and film. The liquid/vapour surface tension of the droplet is denoted by σ_{lv}. So far, electrowetting experiments have been mainly performed with droplets of aqueous electrolyte solutions on polymer coated dielectric films [2.151]. Only recently studies with ionic liquids have been reported [2.152–2.154]. Essentially, they exhibit the same electrowetting features of a parabolic dependence of $\cos\Theta$ vs. U^2 as is observed in electrolyte solutions. However, at higher voltages – ≥ 50 V in [C_4mim][PF_6] and [C_4mim] [NTf_2] melts on a 100 nm SiO_2-Si dielectric substrate – decomposition of these ionic liquids sets in [2.79]. This is presumably caused by an electric breakdown and a corresponding discharging. The decomposition has been observed by the formation of large bubbles under UHV conditions that result from decomposition products such as HF. An example is given in Fig. 2.21.

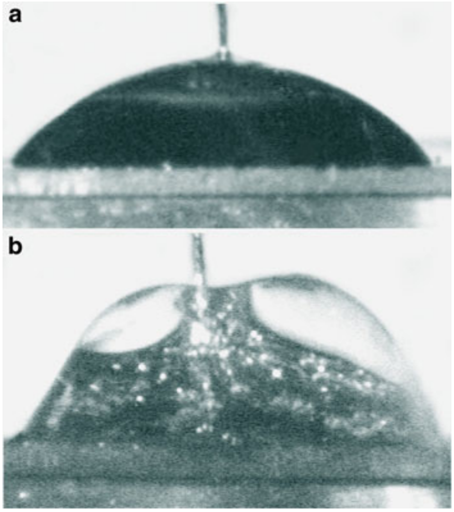

Fig. 2.21 Typical droplet shape of a $[C_4mim][PF_6]$ ionic liquid on a 100 nm thick SiO_2Si substrate with a contact line diameter of ~2.60 mm at 298 K; (**a**) for an applied voltage below 50 V, (**b**) above 50 V where decomposition occurs indicated by small and large bubbles. These measurements have been performed under UHV conditions. Adapted from [2.79]

Table 2.6 Interfacial free energies or surface tensions, σ_{lv}, and their temperature dependence at the liquid/vapour interface of selected molten salts and ionic liquids near their respective melting points

Compound	$\sigma_{\text{lv}}/\text{mJ m}^{-2}$	$-\partial\sigma_{\text{lv}}/\partial T/\text{mJ m}^{-2}\,\text{K}^{-1}$
NaCl	1,138 (a)	0.07 (a)
KCl	98 (a)	0.07 (a)
$BiCl_3$	73 (b)	0.139 (b)
$[C_4mim][Cl]$	47.5 (c)	0.04 (c)
$[C_4mim][Cl]-AlCl_3$ (1:1)	46.5(c) (300 K)	0.055 (c)
$[C_4mim][PF_6]$	43.5 (d)	0.035 (d)

(a) = [2.135], (b) = [2.19], (c) = [2.155], (d) = [2.156]

In concluding this section, a selection of representative values of liquid/vapour surface tensions of molten salts and ionic liquids at conditions near their respective melting points is given in Table 2.6.

References

2.1. H.T. Davis, *Statistical Mechanics of Phases, Interfaces, and Thin Films* (Wiley-VCH, New York, 1996)
2.2. D.M. Heyes, *The Liquid State* (Wiley, Chichester, 1998)
2.3. J.P. Hansen, I.R. McDonald, *Theory of Simple Liquids* (Academic, London, 1976)
2.4. N.W. Ashcroft, N.D. Mermin, *Solid State Physics* (Saunders College, Philadelphia, 1976)

2.5. J. Hafner, *From Hamiltonians to Phase Diagrams* (Springer, Berlin, 1987)
2.6. J.M. Ziman, *Principle of the Theory of Solids* (Cambridge University Press, Cambridge, 1965)
2.7. N.E. Cusack, *The Physics of Structurally Disordered Matter* (Hilger, Bristol, 1987)
2.8. J. Lindhard, Kgl. Danske Videnskab Selska. Mat-Fys. Medd. **28** (1954)
2.9. A. Rahman, Phys. Rev. B **9**, 1667 (1974)
2.10. D.L. Price, K.S. Singwi, M.P. Tosi, Phys. Rev. B **2**, 2983 (1970)
2.11. J.R.D. Copley, J.M. Rowe, Phys. Rev. A **9**, 1656 (1974)
2.12. G. Mamantov, R. Marassi, (eds.), *Molten Salt Chemistry* (D. Reidel, Dordrecht, 1987)
2.13. P. Wasserscheid, T. Welton (eds.), *Ionic Liquids in Synthesis* (Wiley-VCH, Weinheim, 2008)
2.14. R.J. Gale, B. Gilbert, R.A. Osteryoung, Inorg. Chem. **17**, 2728 (1978)
2.15. J.S. Wilkies, J.A. Levisky, R.A. Wilson, C.L. Hussey, Inorg. Chem. **21**, 1263 (1982)
2.16. A.A. Famin, D.A. Floreani, L.A. King, J.S. Landers, B.J. Piersma, D.J. Steck, R.L. Vaughn, J.S. Wilkes, J.L. Williams, J. Phys. Chem. **88**, 2614 (1984)
2.17. E.W.J. Mitchell, P.F.J. Poncet, R.J. Stewart, Phil. Mag. **34**, 72 (1976)
2.18. M. Rovere, M.P. Tosi, Rep. Progr. Phys. **49**, 1001 (1986)
2.19. G.J. Janz, *Molten Salts* (Academic, New York, 1967)
2.20. F.G. Edwards, J.E. Enderby, R.A. Howe, D.I. Page, J. Phys. C:. Solid. State. Phys. **8**, 3483 (1975)
2.21. J.Y. Derrien, J. Dupuy, J. Phys. Paris. **36**, 191 (1975)
2.22. N.H. March, M.P. Tosi, *Coulomb Liquids* (Academic, London, 1984)
2.23. M. Born, K. Huang, *Dynamical Theory of Crystal Lattices* (Oxford University Press, Oxford, 1954)
2.24. M.P. Tosi, F.G. Fumi, J. Phys. Chem. Solids **23**, 45 (1964)
2.25. D.J. Adams, I.R. McDonald, J. Phys. C: Solid State Phys. **8**, 2198 (1975)
2.26. L.V. Woodcock, Chem. Phys. Lett. **10**, 257 (1971)
2.27. L.V. Woodcock, K. Singer, Trans. Faraday Soc. **67**, 12 (1971)
2.28. S. Biggin, J. Enderby, J. Phys. C: Solid State Phys. **15**, L305 (1982)
2.29. J.W. Lewis, K. Singer, L.V. Woodcock, J. Chem. Soc. Faraday Trans. **71**, 41 (1975)
2.30. P. Ballone, G. Pastore, M. Tosi, J. Chem. Phys. **81**, 3174 (1984)
2.31. S. Eisenberg, J.F. Jal, J. Dupuy, P. Chieux, P. Knoll, Philos. Mag. A **46**, 195 (1982)
2.32. W. Andreoni, G. Galli, M.P. Tosi, Phys. Rev. Lett. **55**, 1734 (1985)
2.33. J.E. Enderby, S. Biggin, in *Advances in Molten Salt Chemistry*, vol. 5, ed. by G. Mamantov (Elsevier, Amsterdam, 1983)
2.34. R. Triolo, A.H. Narten, J. Chem. Phys. **74**, 703 (1981)
2.35. D.A. Allen, R.R. Howe, N.D. Wood, W.S. Howells, J. Chem. Phys. **94**, 5071 (1991)
2.36. J. Neuefeind, Phys. Chem. Chem. Phys. **3**, 3987 (2001)
2.37. A.K. Scoper, Phys. Rev. B **72**, 104204 (2005)
2.38. M.H. Brooker, G.N. Papatheodorou, in Advances in Molten Salt Chemistry, vol 5, ed. by G. Mamantov (Elsevier, Amsterdam, 1983)
2.39. E.A. Pavlatou, P.A. Madden, M. Wilson, J. Chem. Phys. **107**, 10446 (1997)
2.40. V.V. Brazhkin, Y. Katayama, A.G. Lyapin, S.V. Propova, Y. Inamure, H. Saitoh, W. Utsumi, JETP. Lett. **83**, 13 (2005)
2.41. R. Roberto, G. Pastore, M.P. Tosi, Phys. Lett. A **373**, 1083 (2009)
2.42. F. Hutchinson, M.K. Walters, A.J. Rowley, P.A. Madden, J. Chem. Phys. **110**, 15821 (1999)
2.43. J.L. Gray, G.E. Maciel, J. Am. Chem. Soc. **103**, 7141 (1981)
2.44. M.P. Tosi, D.L. Price, M.L. Saboungi, in Annual Review Physical Chemistry, vol 44, ed. by H.R. Strauss (Ann Review Inc, Palo Alto, 1993)
2.45. P.A. Hunt, E.J. Magime, R.M. Lynden-Bell, M.G. Del Populo, in Ionic Liquids in Synthesis, ed. by P. Wasserscheid, T. Welton (Wiley-VCH, Weinheim, 2008)
2.46. C.G. Hanke, S.L. Price, R.M. Lynden-Bell, Mol. Phys. **99**, 801 (2001)
2.47. Y. Wang, G.A. Voth, J. Am. Chem. Soc. **127**, 12192 (2005)
2.48. Y. Wang, S. Feng, G.A. Voth, J. Chem. Theor. Comput. **5**, 1091 (2009)
2.49. B.L. Bhargava, M.L. Klein, J. Phys. Chem. A **113**, 1898 (2009)
2.50. C. Spickermann et al., J. Chem. Phys. **129**, 104505/1 (2008)

2.51. R.C. Remsing et al, Abstracts of Paper, 236th ACS National Meeting, Philadelphia (2008)
2.52. A.R. Porter, S.Y. Liem, P.L.A. Popelier, Phys. Chem. Chem. Phys. **10**, 4240 (2008)
2.53. R.C. Remsing, Z. Liu, I. Sergeyev, G. Moyna, Phys. Chem. Chem. Phys. **10**, 4240 (2008)
2.54. C. Schroder, T. Rudars, G. Neumayr, S. Benkner, O. Steinhauser, J. Chem. Phys. **127**, 234503/1 (2008)
2.55. X. Wu, Z. Liu, S. Huang, W. Wang, Phys. Chem. Chem. Phys. **7**, 2771 (2005)
2.56. A. Chaumont, G. Wipff, Inorg. Chem. **48**, 4277 (2009)
2.57. A. Chaumont, G. Wipff, Chem.: A Eur. J. **10**, 3919 (2004)
2.58. C. Hardacre, in *Ionic Liquids in Synthesis*, ed. by P. Wasserscheid, T. Welton (Wiley-VCH, Weinheim, 2008)
2.59. K. Fujii et al., J. Phys. Chem. B **112**, 4329 (2008) and further references therein
2.60. J.R. Wilson, Metall. Rev. **10**, 381 (1965)
2.61. F. Hensel, W.W. Warren, *Fluid Metals – The Liquid-Vapour Transition of Metals* (Princeton University Press, Princeton, 1999)
2.62. W. Freyland, F. Hensel, Ber. Bunsenges Phys. Chem. **76**, 16 (1972)
2.63. G. Treiber, K. Tödheide, Ber. Bunsenges Phys. Chem. **77**, 540 (1973)
2.64. N.N. Greenwood, A. Earnshaw, *Chemistry of the Elements* (Pergamon, Oxford, 1984)
2.65. http://www.wikipedia.org/critical point (thermodynamics)
2.66. G. Raabe, J. Köhler, J. Chem. Phys. **129**, 144503 (2008)
2.67. H. Ohno, in *Electrodeposition from Ionic Liquids*, ed. by F. Endres, D. Mac-Farlane, A. Abbot (VCH-Wiley, Weinheim, 2008)
2.68. R.F. Tournier, Physica. B **392**, 79 (2007)
2.69. D. Turnbull, J. Appl. Phys. **20**, 817 (1949)
2.70. J.H. Perepezko, J.S. Paik, J. Non. Cryst. Solids **61**, 113 (1984)
2.71. J.H. Perepezko, J.S. Paik, Rapid solidified amorphous and crystalline alloys. Conference Proceedings Boston, Boston, MA, 1982
2.72. J.H. Perepezko, P.H. Rasmussen, I.E. Anderson, C.R. Loper, Proceedings of International Conference on Solidification 1977, Boston, MA, 1979
2.73. H. Tostmann, W. Freyland, J. Non-Crystalline Solids, 156–158:**551** (1993)
2.74. W. Freyland, F. Hensel, in *The Metallic and Non-Metallic States of Matter*, ed. by P.P. Edwards, C.N.R. Rao (Taylor and Francis, London, 1985)
2.75. K.H. Simmrock, R. Janowski, A. Ohnsorge, *Critical Data of Pure Substances* (Dechema, Frankfurt/M, 1986)
2.76. D.M. Fox, W.H. Awad, J.W. Gilmann, P.H. Maupin, H.C. De Long, P.C. Trulove, Green Chem. **5**, 724 (2003)
2.77. Y. Shimizu, Y. Ohte, Y. Yamanura, K. Saito, Chem. Phys. Lett. **470**, 295 (2009)
2.78. A.J. Easteal, C.A. Angell, J. Phys. Chem. **74**, 3987 (1970)
2.79. V. Halka, W. Freyland, Z. Phys. Chem. **222**, 117 (2008)
2.80. K.R. Lovelock, C. Kolbeck, T. Cremer, N. Paape, P.S. Schulz, P. Wasserscheid, F. Maier, H.P. Steinbrück, J. Phys. Chem. B. **113**, 2854 (2009)
2.81. L.P.N. Rebelo, J.N. Comingia Lopez, J.M.S. Esperanca, E. Filipe, J. Phys. Chem. B **109**, 6041 (2005)
2.82. J.P. Armstrong, C. Hurst, R.G. Jones, P. Licence, K.R.J. Lovelock, R.G. Satterley, J. Villar-Garcia, Phys. Chem. Chem. Phys. **9**, 982 (2007)
2.83. D.H. Zaitsau, G.H. Kabo, A.A. Strechan, Y.U. Paulechka, A. Tschersich, S.P. Verevkin, A. Heintz, J. Phys. Chem. A. **110**, 7303 (2006)
2.84. V.N. Emel'yanenko, S.P. Verevkin, A. Heintz, J. Am. Chem. Soc. **129**, 3930 (2007)
2.85. P. Scamwells, Aust. J. Chem. **58**, 155 (2005)
2.86. J.V. Senger, J.M.H. Levelt Sengers, Ann. Rev. Phys. Chem. **37**, 189 (1986)
2.87. Y. Levin, X. Li, M.E. Fisher, Phys. Rev. Lett. **73**, 2716 (1994)
2.88. M.E. Fisher J. Phys. Condens Matter 8:9103 (1996)
2.89. A.G. Moreira, M.M. Telo da Gama, M.E. Fisher J. Chem. Phys. 110:10058 (1999)
2.90. Y.C. Kim, M.E. Fisher Chem. Phys. Lett. **414**, 185 (2005)
2.91. S.K. Das, J. Horbach, K. Binder, M.E. Fisher, J.V. Sengers J. Chem. Phys. 125: 024501/1 (2006)

2.92. K.S. Pitzer, J. Phys. Chem. **99**, 13070 (1995)
2.93. T. Narayana, K.S. Pitzer Phys. Rev. Lett. **73**, 3002 (1994)
2.94. K.S. Pitzer, Acc. Chem. Res. **23**, 333 (1990)
2.95. H. Weingärtner, W. Schröer, J. Mol. Liquids. **66**, 107 (1995)
2.96. W. Freyland, in *Metal-Insulator Transitions Revisited*, ed. by P.P. Edwards, C.N.R. Rao (Taylor and Francis, London, 1995)
2.97. P. Chieux, M.J. Sienko, J. Chem. Phys. **53**, 566 (1970)
2.98. J.F. Jal, P. Chieux, J. Dupuy, J.P. Dupin, J. Phys. **41**, 657 (1980)
2.99. H. Weingärtner, T. Merkel, U. Maurer, J.P. Lonzen, H. Glasbrenner, S. Kaeshammer, Ber. Bunsenges Phys. Chem. **95**, 1579 (1991)
2.100. M. Kleemaier, S. Wiegand, W. Schröer, H. Weingärtner, J. Chem. Phys. **110**, 3085 (1999)
2.101. W. Schröer, J. Mol. Liquids. **125**, 164 (2006)
2.102. W.H. Young, A. Meyer, G.E. Kilby, Phys. Rev. **160**, 482 (1967)
2.103. J.E. Enderby, in *Liquid Metals, Chemistry and Physics*, ed. by S.Z. Beer (Marcel Dekker, New York, 1972)
2.104. U. Even, W. Freyland, J. Phys. F **5**, 104 (1975)
2.105. A.A. Dworkin, H.R. Bronstein, M.A. Bredig, J. Phys. Chem. **67**, 2715 (1963)
2.106. S. Zein El Abedin, O. Terakado, F. Endres, D. Nattland, W. Freyland, Phys. Chem. Chem. Phys. **4**, 5335 (2002)
2.107. O. Terakado, P. Poh, W. Freyland, J. Phys. Condens. Matter **15**, 1553 (2003)
2.108. L.F. Grantham, S.J. Yosim, in *Characterization and Analysis*, G. Mamantov ed. by (Marcel Dekker, New York, 1969)
2.109. U. Stöhr, W. Freyland, Phys. Chem. Chem. Phys. **1**, 4383 (1999)
2.110. J.P. Hansen, I.R. McDonald, J. Phys. C Solid State Phys. **7**, L384 (1974)
2.111. A. Noda, M. Watanabe, K. Hayamizu, J. Phys. Chem. B **105**, 4603 (2001)
2.112. N.A. Stolwijk, S. Obeidi, Electrochimica Acta. **54**, 1645 (2009)
2.113. A.W. Adamson, A.P. Gast, *Physical Chemistry of Surfaces*, 3rd edn. (Wiley, New York 1997)
2.114. D.R. Clarke, M. Rühle, A.P. Tomsia (eds.), *Annual Review of Materials Research*, vol 38. (Annual Reviews, Palo Alto, 2008)
2.115. S.A. Rice, J. Gryko, V. Mohanty, in *Fluid Interfacial Phenomena*, ed. by C.A. Croxton (Wiley, New York, 1986)
2.116. B.C. Lu, S.A. Rice, J. Chem. Phys. **68**, 5588 (1978)
2.117. M.J. Regan, E.H. Kawamoto, S. Lee, P.S. Pershan, N. Maskil, M. Deutch, O.M. Magnussen, B.M. Ocko, L.E. Berman, Phys. Rev. Lett. **75**, 2498 (1995); Phys. Rev. Lett. **74**, 444
2.118. P.S. Pershan, S.E. Stoltz, O.G. Shpyrko, M. Deutsch, V.S. Balagurusamy, M. Meron, B. Liu, R. Streitel, Phys. Rev. B **79**, 115417/1 (2009)
2.119. M. Zhao, D.S. Chekmarev, Z.H. Lai, S.A. Rice, Phys. Rev. E. **56**, 7033 (1997)
2.120. A. Gross, *Theoretical Surface Science* (Springer, Berlin, 2003)
2.121. B.C. Allen, in *Liquid Metals,Chemistry and Physics*, ed. by S.Z. Beer (Marcel Dekker, New York, 1972)
2.122. A. Ayyad, W. Freyland, Surf. Sci. **506**, 1 (2002)
2.123. V.K. Kurnikov, K.B. Khokonov, J. Appl. Phys. **54**, 1346 (1983)
2.124. B. Vinet, L. Magnusson, H. Fredriksson, P.J. Desrè, J. Colloid Interface Sci. **255**, 363 (2002)
2.125. H.M. Lu, Q. Jiang, J. Phys. Chem. B **109**, 15463 (2005)
2.126. M.C. Desjonqueres, F. Cyrot-Lackmann, Surf. Sci. **50**, 257 (1975)
2.127. D. Turnbull, Sol. State Phys. **3**, 225 (1956)
2.128. R.M. Digilov, Physica. B **352**, 53 (2004)
2.129. J.W. Cahn, J. Chem. Phys. **66**, 3667 (1977)
2.130. W. Freyland, D. Nattland, Ber. Bunsenges Phys. Chem. **102**, 1 (1998)
2.131. S. Dietrich, Wetting Phenomena. in *Phase Transitions and Critical Phenomena,* vol 12, ed. by C.Domb, J.L. Lebowiz (Academic, London, 1988)
2.132. M. Rauscher, S. Dietrich, Wetting Phenomena in Nanofludics, in *Annual Review of Materials Research*, vol 38, ed. by D.R. Clarke, M. Rühle, A.P. Tomsia (Annual Reviews, Palo Alto, 2008)

2.133. D. Bonn, J. Eggers, J. Indekeu, J. Meunier, E. Rolley, Rev. Mod. Phys. **81**, 739 (2009)
2.134. M.M. Telo da Gama, R. Evans, T.J. Sluckin, Mol. Phys. **41**, 1355 (1980)
2.135. R. Evans, T.J. Sluckin, Mol. Phys. **40**, 413 (1980)
2.136. D.M. Heyes, J.H.R. Clarke, J. Chem. Soc. Faraday Trans. **77**, 1089 (1981)
2.137. D.M. Heyes, Phys. Rev. B **30**, 1282 (1984)
2.138. G. Navasmés, P. Tarazona, Mol. Phys. **37**, 1077 (1979)
2.139. U. Tartaglino, T. Zykova-Timan, F. Ercolessi, E. Tossati, Phys. Rep. **411**, 291 (2005)
2.140. G. Grange, B. Mutaftschiev, Surf. Sci. **47**, 723 (1975)
2.141. T. Zykova-Timan, D. Ceresoli, U. Tartaglino, E. Tosatti, Phys. Rev. Lett. **94**, 176105–1 (2005)
2.142. R.M. Lynden-Bell, Mol. Phys. **101**, 2625 (2003)
2.143. B.L. Bhargava, S. Balasubramanian, J. Am. Chem. Soc. **128**, 10073 (2006)
2.144. P.G. Law, P.R. Watson, A.I. Carmichael, K.R. Seddon, Phys. Chem. Chem. Phys. **3**, 2879 (2001)
2.145. S. Rivera-Rubero, S. Baldelli, J. Am. Chem. Soc. **126**, 11788 (2004)
2.146. E. Sloutskin, B.N. Ocko, L. Tamann, L. Kuzmenko, T. Gog, M. Deutsch, J. Am. Chem. Soc. **127**, 7796 (2005)
2.147. Y. Jeon, J. Sung, W. Bru, D. Vaknin, Y. Ouchi, D. Kim, J. Phys. Chem. C. **112**, 19649 (2008)
2.148. I. Langmuir, Science **88**, 430 (1938)
2.149. S. Staroske, W. Freyland, D. Nattland, J. Chem. Phys. **115**, 7669 (2001)
2.150. M. Mezger, H. Schröer, H. Reichert, S. Schramm, J.S. Okasinski, S. Schöder, V. Honkimaki, M. Deutsch, B.M. Ocko, J. Ralston, M. Rohwerder, M. Stramann, H. Dosch, Science **322**, 424 (2008)
2.151. F. Mugele, J.C. Baret, J. Phys. Condens. Matter. **17**, R705 (2005)
2.152. P. Dubois, G. Marchand, Y. Fouillet, J. Berthier, T. Douki, F. Hassine, S. Gmout, M. Vaultier, Anal. Chem. **78**, 4909 (2006)
2.153. S. Millefiorini, A.H. Tkaxzyk, R. Sedev, J. Efthimiais, J. Ralston, J. Am. Chem. Soc. **128**, 308 (2006)
2.154. Y. Sato, T. Ejima, M. Fukasawa, K. Abe, J. Phys. Chem. **94**, 1991 (1990)
2.155. V. Halka, R. Tsekov, W. Freyland, J. Phys. Condensed Matter **17**, S3325 (2005)
2.156. V. Halka, R. Tsekov, W. Freyland, Phys. Chem. Chem. Phys. **7**, 2038 (2005)